

Flexible and Stretchable Capacitive Sensors with Different Microstructures

Jing Qin, Li-Juan Yin, Ya-Nan Hao,* Shao-Long Zhong, Dong-Li Zhang, Ke Bi, Yong-Xin Zhang, Yu Zhao, and Zhi-Min Dang*

Recently, sensors that can imitate human skin have received extensive attention. Capacitive sensors have a simple structure, low loss, no temperature drift, and other excellent properties, and can be applied in the fields of robotics, human–machine interactions, medical care, and health monitoring. Polymer matrices are commonly employed in flexible capacitive sensors because of their high flexibility. However, their volume is almost unchanged when pressure is applied, and they are inherently viscoelastic. These shortcomings severely lead to high hysteresis and limit the improvement in sensitivity. Therefore, considerable efforts have been applied to improve the sensing performance by designing different microstructures of materials. Herein, two types of sensors based on the applied forces are discussed, including pressure sensors and strain sensors. Currently, five types of microstructures are commonly used in pressure sensors, while four are used in strain sensors. The advantages, disadvantages, and practical values of the different structures are systematically elaborated. Finally, future perspectives of microstructures for capacitive sensors are discussed, with the aim of providing a guide for designing advanced flexible and stretchable capacitive sensors via ingenious human-made microstructures.

exhibits characteristics such as a low modulus, high toughness, and high tear resistance.^[3,4] The powerful sensing system of the skin can help the human body sense pressure, deformation, temperature, humidity, and other stimuli, and transmit these changes to the brain in the form of different electrical signals.^[5,6] The human body relies on these sensory inputs from the skin and the proprioception of muscles, tendons, joints, and other motor organs in different states to maintain normal posture and complete the basic activities of daily life.^[7,8] Electronic skin (E-skin) is a flexible electronic device that simulates the human skin sensing mechanism by converting physiological signals into electronic signals (**Figure 1**).^[6,9–12] Compared with traditional rigid electronic devices, flexible and stretchable E-skin has significant practical value in human–machine interactions, Internet of Things (IoT), and other application fields.^[10,13,14] With the rapid development of technolo-

1. Introduction

As the largest organ in the human body, the skin plays an important role in daily life.^[1,2] Based on the collaboration of the two main components, collagen and elastin fibers, the skin


gives such as artificial intelligence and soft robots, requirements for materials used in human–machine interfaces have also gradually increased. These materials must imitate the mechanical properties of human skin tissues, establish information transmission networks, interact intelligently with the external environment, and be capable of sensing multiple stimuli and can greatly promote the development of sensors.^[2,15–17]

According to the operating mechanism, sensors can be divided into three categories: piezoelectric, resistive, and capacitive.^[18,19] The advantages and disadvantages of these common sensors types are compared in **Table 1**. Parameters such as the length and distance between the dipoles in the piezoelectric sensor change with the applied force, resulting in an increase in the charge and voltage.^[20–23] Therefore, piezoelectric sensors require no additional power supply. They have a high sensitivity and a fast response speed to dynamic pressure. However, they cannot detect static loads and can drift over time in a sensor response with erratic reliability.^[24,25] According to the resistance calculation formula $R = \rho \frac{L}{S}$, where ρ is the resistivity, L is the length, and S is the cross-sectional area, and the force applied changes in the material's geometry, namely, L and S when ρ is unchanged, thus changing the material's resistance R .^[26] Resistive sensors are easy to manufacture at low cost, which are currently the most studied sensors.^[27,28] However, the resistivity of various materials generally varies with temperature,^[29,30] which

J. Qin, L.-J. Yin, Dr. S.-L. Zhong, Dr. D.-L. Zhang, Y.-X. Zhang,
Prof. Z.-M. Dang
State Key Laboratory of Power System
Department of Electrical Engineering
Tsinghua University
Beijing 100084, China
E-mail: dangzm@tsinghua.edu.cn

J. Qin, Prof. Y.-N. Hao, Prof. K. Bi
State Key Laboratory of Information Photonics
and Optical Communications
School of Science
Beijing University of Posts and Telecommunications
Beijing 100876, China
E-mail: hyn@bupt.edu.cn

Dr. Y. Zhao
School of Electrical Engineering
Zheng Zhou University
Zhengzhou, Henan 450001, China

 The ORCID identification number(s) for the author(s) of this article can be found under <https://doi.org/10.1002/adma.202008267>.

DOI: 10.1002/adma.202008267

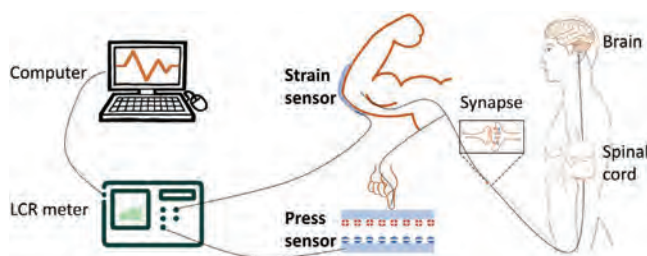


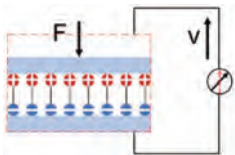
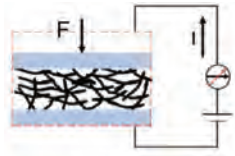
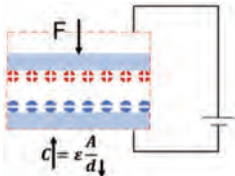
Figure 1. Schematic illustration of signal conversion in human feedback system and E-skin.

makes them easily affected by temperature or humidity changes in the external environment.^[31,32] Resistive sensors may also be affected by environmental factors or via contact with the human body (e.g., sweat and body fluids) when applied in a wearable system, causing drift and deteriorating the stability and reliability of data output.^[33] If the fringing of the electric field is negligible, the capacitance of the plane-parallel capacitor can be expressed as $C = k_0 k_r \frac{A}{d}$, where k_0 is the free-space permittivity, k_r is the relative permittivity of the dielectric material, A is the area of the parallel electrodes, and d is the distance between the two parallel electrodes.^[34] In comparison, the effect of temperature and humidity on the dielectric constant is smaller than that on the conductivity. Hence, this type of temperature drift hardly occurs in capacitive sensors. When materials with a low-temperature coefficient are selected as the electrodes of the capacitive sensors, their temperature coefficients are extremely small and are almost unaffected by temperature.^[32] In addition, capacitive sensors have the advantages of simple device structure, low power consumption, low detection limit, wide application range, fast dynamic response, and durability,^[35–41] which have been extensively studied and applied in E-skin,^[42,43] medical prosthetics,^[44] wearable devices,^[13,45] biometrics,^[38,46] touchpads and touch screens,^[47–49] and other consumer electronics fields.^[47,50–53]

In the past few decades, various methods for fabricating flexible capacitive sensors have been proposed. The early preparation methods of capacitive sensors are mostly based on micro-electromechanical system (MEMS) technology.^[54] However, semiconductor-based devices have poor mechanical properties, are hard and brittle, and cannot withstand large deformations. Therefore, to replace silicon-based materials, various polymer-based materials, such as polydimethylsiloxane (PDMS),^[44,55–63] Ecoflex,^[31,51,64–71] and polyurethane (PU),^[66,72–76] have been proposed and widely used as flexible substrates for capacitive sensors. These polymers have a low Young's modulus and a high degree of stretchability.^[77–79] In addition to good elasticity and toughness, chemical stability, and transparency, they also have desirable biocompatibility^[36,80] and electrical insulation.^[74] However, the unchanged volume of the polymer dielectric layer limits the improvement in sensitivity.^[37,39] Most polymer elastomers have severe viscoelasticity and interfacial adhesion,^[55,81] which increase the hysteresis and reduce the response speed of the device.^[51,82] In practical applications, especially in biomedicine, the response time affects the speed of signal collection and processing.^[40,41] High hysteresis may fail to accurately reflect the patients' physical conditions in real time, which will lead to a delay in treatment time.

To solve this problem, numerous researchers have designed different microstructures to achieve greater strain of the elastomer, thereby enhancing the sensing range.^[83] Both Guo and co-workers and Zhang and co-workers used microstructured PDMS as the dielectric layer, which proved that the distance and capacitance change of the sensor with microstructured PDMS are tens of times higher than those of sensors with nonstructured PDMS.^[55,84] The Young's modulus, sensitivity, and stretchability can be improved by adding various artificially designed microstructures fabricated of different materials. Park et al. designed microstructures to expand the failure strain (from 240% to 400%), low modulus, and large ratio of capacitance change (from 0.25 to 1.5).^[56] The presence of air in the

Table 1. Comparison of the three common sensors.

Category	Mechanism	Advantages	Disadvantages
Piezoelectric sensors		Self-power ability Simple structure High sensitivity to dynamic pressure Fast response speed	Unable to static sensing Drift over time Lower reliability
Resistive sensors		Low-cost Simple fabrication techniques Most studied	Hysteresis effect Temperature dependent Humidity dependent
Capacitive sensors		Simple structure Temperature independent Low power consumption Low-pressure detection limit Fast dynamic response	Low sensitivity Susceptible to environmental interference

microstructures enables the surface to elastically deform when pressure is applied, which can store and release energy reversibly, thereby greatly reducing the effect of the viscoelasticity of the matrix and helping the sensors to recover quickly during the load–release process.^[36] Finite element analysis (FEA) of hyperelastic materials based on electromechanical coupling simulation also proves that the usage of microstructures is essential for sensors to achieve high sensitivity.^[51]

Herein, two types of sensors—pressure sensors and strain sensors—are discussed based on the application of external forces. First, we introduce five microstructures currently used in pressure sensors. We also compare and analyze the effects of different structures on improving the sensitivity, linearity, and other performances (Section 2). Then, the four microstructures in the strain sensor are discussed, compared, and analyzed to determine how different microstructures improve the stretchability of strain sensors and the practical application value of strain sensors (Section 3). Finally, future development trends and challenges associated with flexible and stretchable capacitive sensors are proposed in this review (Section 4).

2. Bendable Pressure Sensors

Pressure sensing is one of the most important functions of the human skin.^[19] Diverse types of sensory receptors with different sizes, shapes, quantities, and distributions exist on the human skin to realize various features of pressure perception in different parts of the skin.^[11] For example, the skin on the fingers and that on the body have different sensory fields and sensitivities. Physiological pressure changes may also reflect deterioration of body tissue due to diseases.^[85] Through the signal conversion of sensors, we can predict the underlying diseases in the body in advance to control development of the disease. To endow E-skin with the ability of pressure perception, pressure sensors with different sensitivity and pressure ranges have been extensively studied to satisfy diverse application scenarios.

Generally, the performance of sensors is related to their capacitance and structure. If the fringing of the electric field is negligible, the capacitance of the plane-parallel capacitor can be expressed as^[68,71,86–90]

$$C = k_0 k_r \frac{A}{d} \quad (1)$$

where $k_0 (=8.85 \times 10^{-12} \text{ F m}^{-1})$ is the free space permittivity, k_r is the relative permittivity of the polymer dielectric, A is the area of the parallel electrodes, and d is the distance between the two parallel electrodes. Because the Poisson's ratio of the polymer film is relatively large, the volume does not change when force is applied. When pressure p is applied, the capacitive sensor undergoes mechanical deformation, and the thickness d of the dielectric layer can be calculated by the following formula (when the deformation is less than 10%)^[90]

$$p = -\frac{E(d-d_0)}{d_0} \quad (2)$$

where E is the compressive elastic modulus of the polymer, thus, Equation (1) can be rewritten as^[90]

$$C = k_0 k_r \frac{A_0}{d_0} \frac{E^2}{(E-p)^2} \quad (3)$$

Similar results obtained by the simulation calculations from Bao's group also indicate that the low compression modulus of the polymer film has a significant effect on the improvement in capacitance change and sensitivity.^[67,91] Therefore, ideal flexible sensors should be as soft as possible so that d will be sensitive to external stimuli. Beker et al. reduced the amount of curing agent in PDMS (50:1) to decrease the modulus of the film, which has a higher capacitance change and higher sensitivity than a traditional PDMS film (10:1) under the same pressure.^[91] As shown in **Figure 2A**, the slopes of the two tangents represent sensitivity S at points A and B, respectively, and the calculation equation is as follows^[36]

$$S = \frac{\delta(\Delta C / C_0)}{\delta p} \quad (4)$$

where p is the applied load pressure, ΔC is the difference between the sensor capacitance values before and after the pressure applied, and C_0 is the initial capacitance value. According to Equation (4), when the capacitance ΔC is high under per unit load p , the sensitivity will increase.

For the sensor without a microstructure, capacitance is mainly affected by the decrease in the distance between the two electrodes because the flat contact surface has almost no change with uniform stress distribution under external force.^[57] Significant flexibility is observed in numerous current flexible electronic devices by reducing the thickness d of the substrate; however, such a method is not ideal for improving sensitivity.^[10] Although pure polymer films are indeed much easier to bend, the unchanged volume limits the improvement in sensitivity and pressure range.

To promote sensitivity, Bao's group first proposed the design of adding a microstructure to the pressure sensor in 2010.^[36] By adding a small microstructure in the PDMS dielectric layer, the pressure sensitivity was increased by more than 30 times compared with an unstructured PDMS layer of the same size. There are two main reasons for the significant increase in sensitivity: i) the presence of many voids in the microstructure film is conducive to a smaller elastic modulus and can provide a larger deformation space under the applied pressure, which means that the distance between two electrodes can change more to further increase ΔC under the same pressure;^[36,41,78,94,95] ii) the dielectric constant of the polymer matrix (e.g., $k_{\text{PDMS}} \approx 3.0$) is higher than that of air (≈ 1).^[36,62] When compression occurs, the air volume is occupied by the matrix, and ΔC increases accordingly.^[62,96,97] Therefore, adding microstructures can significantly improve the sensitivity of the sensors.^[98,99] In addition, the microstructure can also reduce the elastic modulus^[100,101] and viscoelasticity, which contributes to reducing the heat loss caused by the resistance and mechanical loss due to the adhesion between the polymer dielectric layer and the electrode layer during the load/release process. Recent research reports have already confirmed that the microstructured or patterned

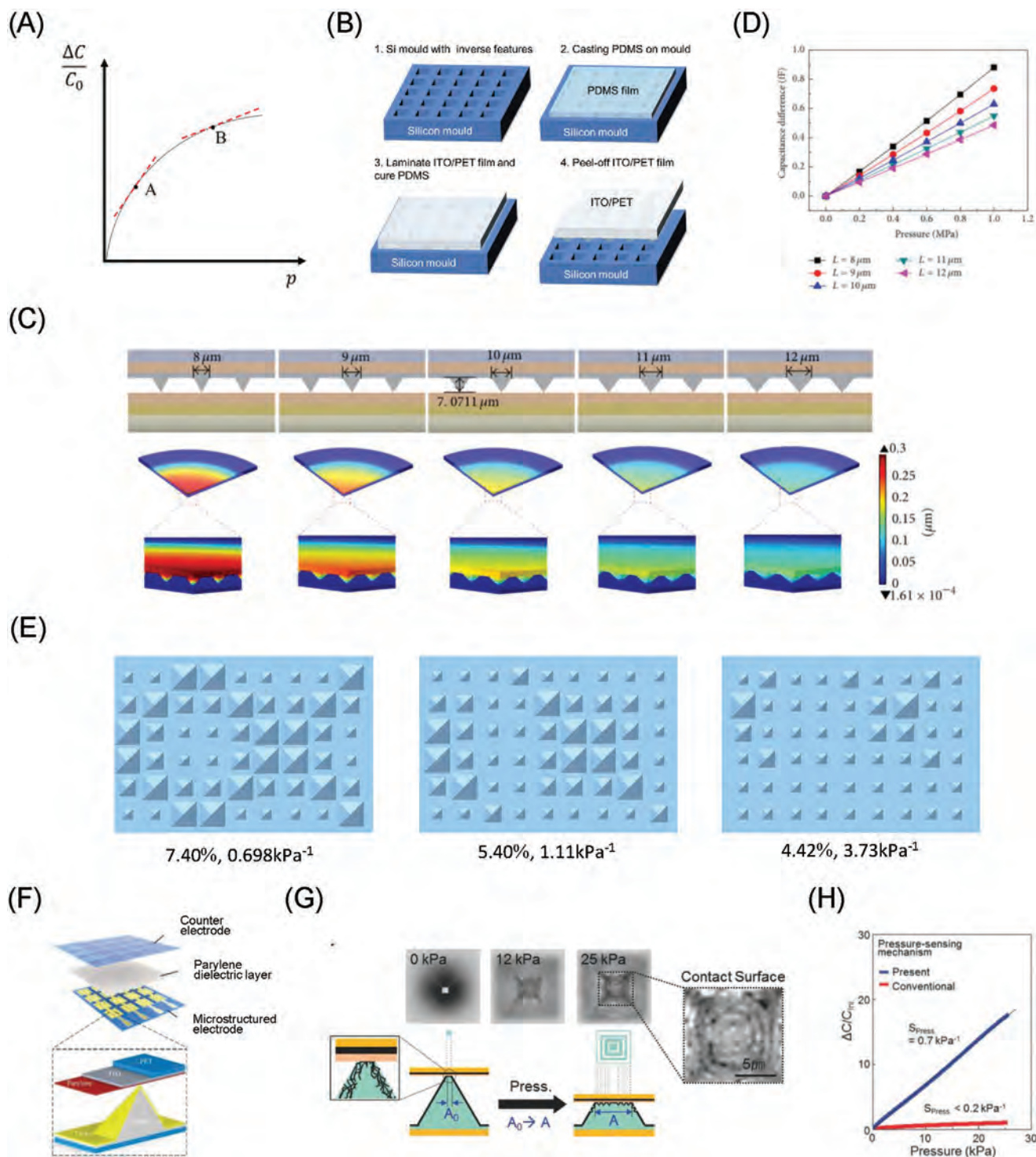


Figure 2. A) Schematic illustration of sensitivity. B) Schematic process for the fabrication of microstructured PDMS films. C) The pressure responses of the capacitive pressure sensors with different lengths of hemline of pyramids. D) The comparison of capacitance–pressure characteristics of the sensors with different lengths. A–D) Reproduced under the terms of the CC-BY Creative Commons Attribution 4.0 International license (<https://creativecommons.org/licenses/by/4.0>).^[92] Copyright 2016, The Authors, published by Hindawi Publishing Corporation. E) Schematic of the differently designed pyramid microstructures for bottom electrodes of the pressure sensor. Data: left-hysteresis, right-sensitivity. F) Illustration of the capacitive pressure sensor based on a microstructured electrode. E,F) Adapted under the terms of the CC-BY Creative Commons Attribution 4.0 International license (<https://creativecommons.org/licenses/by/4.0>).^[51] Copyright 2020, The Authors, published by MDPI. G) Schematic illustration of the pressure-sensing mechanism (contact area variable capacitive). H) Pressure–response curves for present and conventional pressure-sensing mechanism. G,H) Adapted with permission.^[93] Copyright 2018, Wiley-VCH.

dielectric/electrode layer is an ideal and effective approach for strengthening sensor sensitivity.^[102]

2.1. Micropyramid Structure

In 2010, Bao's group first developed a high-sensitivity capacitive pressure sensor by assembling a dielectric layer with a microstructure.^[36] A silicon wafer with an inverted pyramid structure was used as the template. Liquid PDMS was poured into the pyramid structure. After curing, the cured PDMS was separated from the mold to obtain a dielectric layer with a microstructure (Figure 2B). Finally, indium tin oxide polyethylene terephthalate (ITO-PET) was vapor-deposited as electrodes to prepare the sensor. Because the microstructured dielectric layer is highly compressible, the sensitivity of the sensor (maximum sensitivity: 0.55 kPa^{-1} in the range of 0.2 kPa) was 30 times higher than that of unstructured sensors.^[36] The advantage of the micropyramid structure is that the stress is not uniformly distributed with stress concentrated at the tip of the pyramid.^[103] The local stress concentration leads to large structural deformation and consequently high sensitivity.^[104] Owing to its high sensitivity and easy tuning, the micropyramid structure has become the most widely studied and applied microstructure in the field of capacitive pressure sensors.

Since then, many improved methods have been proposed for optimizing the parameters of micropyramids in the study of microstructures. The sensitivity, sensing range, and other related properties can be tuned by modifying the shape of the micropyramids. The relationship curve between the sensitivity and the PDMS pyramids at different spacings was simulated using numerous theoretical calculation models, which confirmed that the pyramid interval was the main factor affecting the capacitive sensor. The sensitivity increases with an increase in spacing because sensors with a lower density of micropyramids exhibit an increased fraction of air, resulting in a large compressibility with a lower Young's modulus and consequently high deformation.^[101,103,105,106] However, the spacing between adjacent cones affects the hysteresis of the response time due to the interfacial adhesion of the polymer matrix.^[106] Capacitive pressure sensors with different sizes of the microstructure were developed using the FEA method. When the distance between two parallel electrodes is constant, the height of the pyramid (H) is fixed. If the L/H ratio of the pyramid decreases (where L is the bottom side length of the pyramid), the angle of the pyramid top decreases and the structure of the pyramid will become sharper. Accordingly, the proportion of the air part increases, and the bendability of the device is improved. Therefore, when the same pressure is applied, the mechanical deformation of the pyramid increases (the spacing between the two electrodes is shortened further), resulting in a larger increase in capacitance and higher sensitivity. The results show that the smaller the L/H ratio of the pyramid is, the sharper the pyramid is and the better the sensitivity will be.^[92,101] This can be explained by the stress distribution of the pyramid (Figure 2C).^[92] Furthermore, because the micropyramid-structured dielectric layer with a smaller or larger L/H ratio behaves more like an unstructured polymer matrix, the sharper pyramid structures produce less hysteresis.^[107] Moreover, less polymer

means that the dielectric layer contains more air, which contributes to a greater volume change and higher sensitivity at lower pressure (Figure 2D).^[92] Cheng et al. designed a hierarchical microstructured electrode with a combination of large and small pyramids to obtain high sensitivity (3.73 kPa^{-1}) and low hysteresis (4.42%) (Figure 2E).^[106] The few large pyramids improve the sensitivity, whereas the small pyramids reduce hysteresis due to interface adhesion. Nevertheless, such a sharp and small structure will result in nonlinearity of the high-pressure range.^[36,58,65,84,100,107–112] The sharply protruding part of the microstructure can be easily compressed under an external force; however, as the load increases, the deformability of the microstructure becomes poor and the equivalent elastic modulus increases. The proportion of the flexible substrate in the dielectric layer and the contact area between the opposite layer in the microstructured sensors tends to be saturated, leading to higher sensitivity in the low-pressure region accompanied by nonlinearity in the high-pressure region. When the L/H ratio of the pyramid is $\approx \sqrt{2}$ (the top angle of the pyramid is 54.7°), the sensor can attain a balance between sensitivity and linearity.^[92,101,107]

Owing to the different thermal expansion coefficients of metal electrodes and polymer substrates, wrinkles and cracks are generated on the metal-film electrodes when deposited on polymer films.^[42,43] Li et al. solved this problem by bonding PET with an ITO electrode on the PDMS film during the metal evaporation process. PET substrates with a lower thermal expansion coefficient and a higher Young's modulus eliminated the thermal expansion of the PDMS structure (Figure 2F).^[51] Although ITO-PET electrodes exhibit good electrical conductivity and high light transmittance, the large elastic modulus limits the compressibility and sensitivity of the sensor. Unlike the traditional mechanism of using the distance change between two electrodes to create a capacitance change, Bae et al. used the feature of the single-walled carbon nanotube (SWCNT)/PDMS mismatch to create micrometer-level wrinkles on the micropyramids under external pressure (Figure 2G). The change in contact area between the microstructured layer and the opposite layer affected the capacitance change; thus, a linear relationship was observed in the dielectric layer as the pressure increased (Figure 2H).^[93] However, this design cannot be employed to control the size and distribution uniformity of the micrometer-level wrinkles and cannot be applied to mass production.

2.2. Microneedle/Pillar Structure

If the L/H ratio of the micropyramid structure increases infinitely, a similar microneedle structure will be obtained. The tip area of the microneedle structure is smaller and the stress is more concentrated than that of the micropyramid structure, and sensors with microneedles have large compressibility, which can help achieve greater mechanical deformation under the same pressure.^[101,113] The distance between the two electrodes is smaller under pressure, resulting in a larger increase in capacitance and higher sensitivity (Figure 3A).^[39,54,55,101,113] For example, under the same pressure of 25 kPa , the increment in capacitance of sensors with a single-sided micropillar

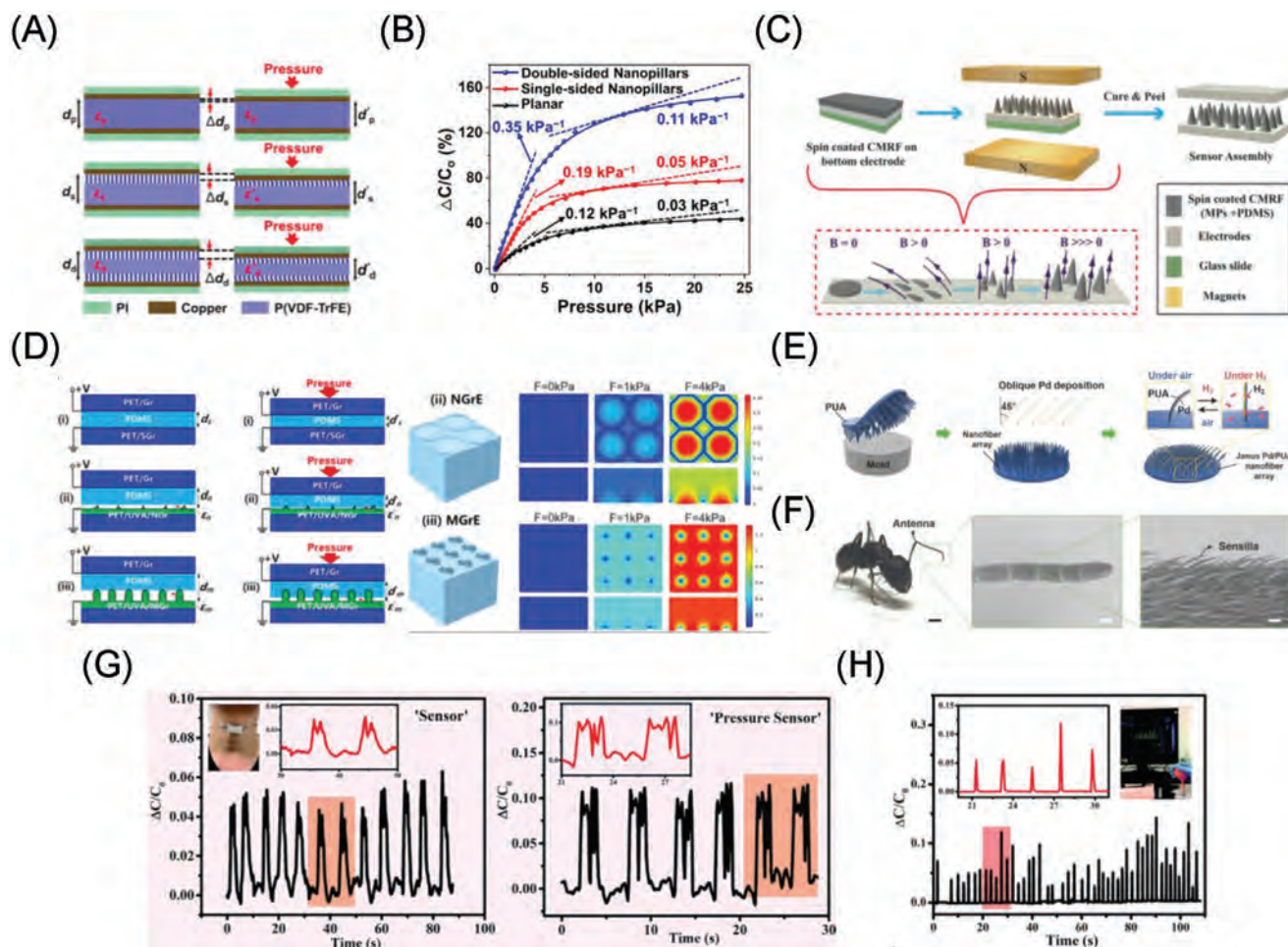


Figure 3. A) Schematic illustration of the variations in the separation distance and the dielectric constant for different capacitive pressure sensors. B) Relative capacitance variation of three sensors constructed by different microstructures. A,B) Reproduced with permission.^[39] Copyright 2019, American Chemical Society. C) Schematic illustration for the fabrication of MGDI-incorporated pressure sensor. The inset figure shows the MGDI formation by changing magnitude and direction (angle) of B_{curing} , higher magnetic field results in large size, less dense needles, and vice versa. Reproduced with permission.^[113] Copyright 2020, Wiley-VCH. D) Geometrical change during the loading process and finite-element simulation showing the local stress distribution and deformation of capacitive pressure sensor based on SGrE, NGrE, and MGrE. Reproduced with permission.^[114] Copyright 2019, American Chemical Society. E) Schematic illustration of the microhair array fabrication procedure. F) Photograph of an ant and SEM images of its antenna composed of high aspect ratio slanted sensilla. Scale bars from left to right: 1 mm, 100 μm , and 10 μm . E,F) Adapted with permission.^[115] Copyright 2017, Wiley-VCH. G) Real-time monitoring of voice vibration during the pronunciations of the "sensor" and "pressure sensor." H) Real-time response measurement and relative capacitance change of the pressure sensor to the airflow. G,H) Adapted with permission.^[116] Copyright 2019, Royal Society of Chemistry.

structure was 70%, whereas that of sensors with a double-sided micropillar structure was 150% because of the large distance variation Δd , which was nearly four times as high as that of sensors without a microstructure (Figure 3B).^[39] To achieve the appropriate balance between precision, cost, and speed, Li's group designed a novel, large-area compatible, and mold-free technology that used a magnetically grown dielectric interface (MGDI) to manufacture flexible pressure sensors with high-aspect-ratio microneedles by optimizing the concentration of magnetic particles (MPs) and the vertical curing magnetic field (B_{curing}) intensity (Figure 3C).^[113] In addition, graphene has been widely employed to improve sensor sensitivity because of its excellent electrical properties in capacitance sensors with a microneedle structure. Yang et al. designed layer microstructured graphene electrodes (MGrEs) as the bottom and top

electrodes in an asymmetrical sandwich sensor; a high sensitivity of 7.68 kPa^{-1} could be obtained in the two-layer MGrEs (Figure 3D) because the roughness and compressibility of electrodes was improved, which is hundreds times higher than that of sensors with smooth graphene electrodes and ten times that of sensors with nanostructured graphene electrodes.^[114] However, when shear forces occur, the microneedle structure layer may slip to a certain extent with the relatively flat electrode layer, which can reduce the robustness of the sensor and limit its measurement range.

Bionic cilia, a special microneedle structure, considerably mimics small hair on the surface of human skin (Figure 3E).^[115] Pang et al. designed a pressure sensor using microhair.^[38] This microhair-structured PDMS interface layer provided the skin with biocompatibility and enhanced the signal-to-noise ratio

(SNR) of the sensor by changing the effective contact between the sensor and the irregular surface of the epidermis. Hairy structures in animals are more sensitive than the human epidermis, which helps them recognize the airflow and perceive the existence of other organisms in the external environment (Figure 3F).^[115,117] Zhou et al. prepared a pressure sensor with cilia arrays imitating the human epidermis by embedding AgNWs into PDMS, which could be used for speech recognition (Figure 3G) and airflow monitoring (Figure 3H), expanding the application range of the sensor.^[116] Although the output pressure capacitance curve of this device remains linear in the range of 0–12 kPa, the data showed nonlinearity in the range of 0–200 kPa. This feature is similar to the nonlinear mechanical behavior of human skin,^[3] however, which is unfavorable to the deformation degree of the object, thereby limiting the application of sensors with microneedle structures.

2.3. Microdome Structure

The microdome structure can endow the sensor with the ability to distinguish between different forces. This hemispherical structure can generate specific deformations according to the type and direction of the applied force, which detects and distinguishes various mechanical stimuli, including pressure, shear, bending, and torsion.^[118–120] Takahashi et al. simulated the variation principle of capacitance change in a microdome sensor using a simplified flow model (Figure 4A).^[121] It was equipped with a novel capacitive force sensor with a polymer dome structure containing silicone oil instead of fragile electrodes at the location of the applied force. When pressure was applied, the oil was pushed into the surrounding thin channel, and the changes in capacitance due to the inflowing dielectric oil were measured between the top and bottom electrodes of the channel.^[121]

Xiong et al. fabricated a microdome PDMS electrode layer with a large deformation in both the distance between two electrodes d and the changed contact area A (Figure 4B).^[57] The experiment and FEA indicated that d and A synergistically caused a significant increase in the capacitance, leading to an observable improvement in its sensitivity (30.2 kPa^{-1}) (Figure 4C).^[57] Compared with the unstructured electrode layers, the discontinuous microstructure has more concentrated stress under the same pressure conditions, resulting in a larger stress concentration and mechanical deformation, eventually improving the sensitivity of the sensor.^[57,74] Beccai's group applied FEM to create a simplified model of a double-layer microdome structure to evaluate the deformation and stress distribution of different microdome shapes, which proved that the ability to distinguish normal and shear forces can be achieved by adjusting various parameters (Figure 4D).^[123] Boutry et al. designed a hierarchically patterned, bioinspired E-skin by combining micropylramids with microdomes (Figure 4E), which also proved that the microdome could detect the direction of applied pressure (Figure 4F).^[74] In addition, they fabricated new biomimetic E-skins with phyllotaxis spiral grids inspired from botany to combine high sensitivity and a fast time response (Figure 4G).^[74] Similar to this double-microstructured sensor, Cheng et al. presented a polymer-based capacitive sensing array

integrating a microdome and hole, which could measure the normal and shear force based on changes in the air gap and capacitance of the cells on sensing elements (Figure 4H).^[122]

However, the microdome structure may cause a sharp reduction in sensitivity as the load increases. The microstructure layer will contact the corresponding electrode layer with the applied pressure, and the sharp tip of the pyramid has a small contact area with the corresponding electrode; thus, the load change can be sensed in real time. In contrast, the semicircular structure at the top of the microdome is relatively smooth. As the contact area increases when a load is applied, the stress will evenly be distributed throughout the microstructure, rather than being concentrated on the sharp top like the micropylramid structure, which leads to insensitivity of the sensor to pressure changes. As the load increases, the semicircular structure is rapidly flattened (Figure 4I), which also reduces its deformability and linear range. Therefore, the pressure response of the sensor with microdomes is similar to that of a sensor without a microstructure.^[124]

2.4. Microporous Structure

Natural multilayer porous structures are abundant in mushrooms, diatoms, and sponges (Figure 5A).^[125] Such a large number of porous structures enable them to have a sufficient elastic deformation space under external forces,^[62] which can provide a large pressure sensing range from several pascals to tens of kilopascals.^[94] The air trapped in the holes with a closed-cell structure acts as a spring.^[81] When an external force is applied, the thin columns between the two pores undergo buckling, and the critical buckling force is inversely proportional to the length of the thin column.^[126,127] Therefore, a large hole with a large deformation has a small compression modulus, resulting in high sensitivity.^[125,128] A device with a porous dielectric structure has high compressibility, fast rebound speed, and a large linear pressure range.^[124] Moreover, the volume fraction of air in this porous structure is so high that the sensor is ultralight^[129] and causes almost no hindrance in daily life activities. In addition, the porous structure has good permeability because of which the normal excretion functions of human skin (e.g., excretion of sweat and body fluids) are not affected and the occurrence of allergies is reduced.^[130] Therefore, polymer foams imitating natural structures have greater mechanical deformability than bulk polymers, and can be employed for heat insulation, vibration damping, and pressure absorption in the automotive and construction industries.^[131]

The manufacture of molds with microstructures is not suitable for low-cost large-area production. For example, micropylramids usually require complex photolithography, chemical etching,^[38,134–136] and subsequent processes with multiple steps, such as demolding. In contrast, the methods for preparing porous structures are usually simple; for example, pores left by sugar dissolved in water (Figure 5B);^[52,71,137] by water volatilized at a high temperature, which does not affect other materials such as the polymer matrix (Figure 5C);^[47,130] and by heating ammonium bicarbonate (NH_4HCO_3), the foaming agent commonly used in the food industry, which produces carbon dioxide (CO_2) after heating (Figure 5D).^[132] These methods are

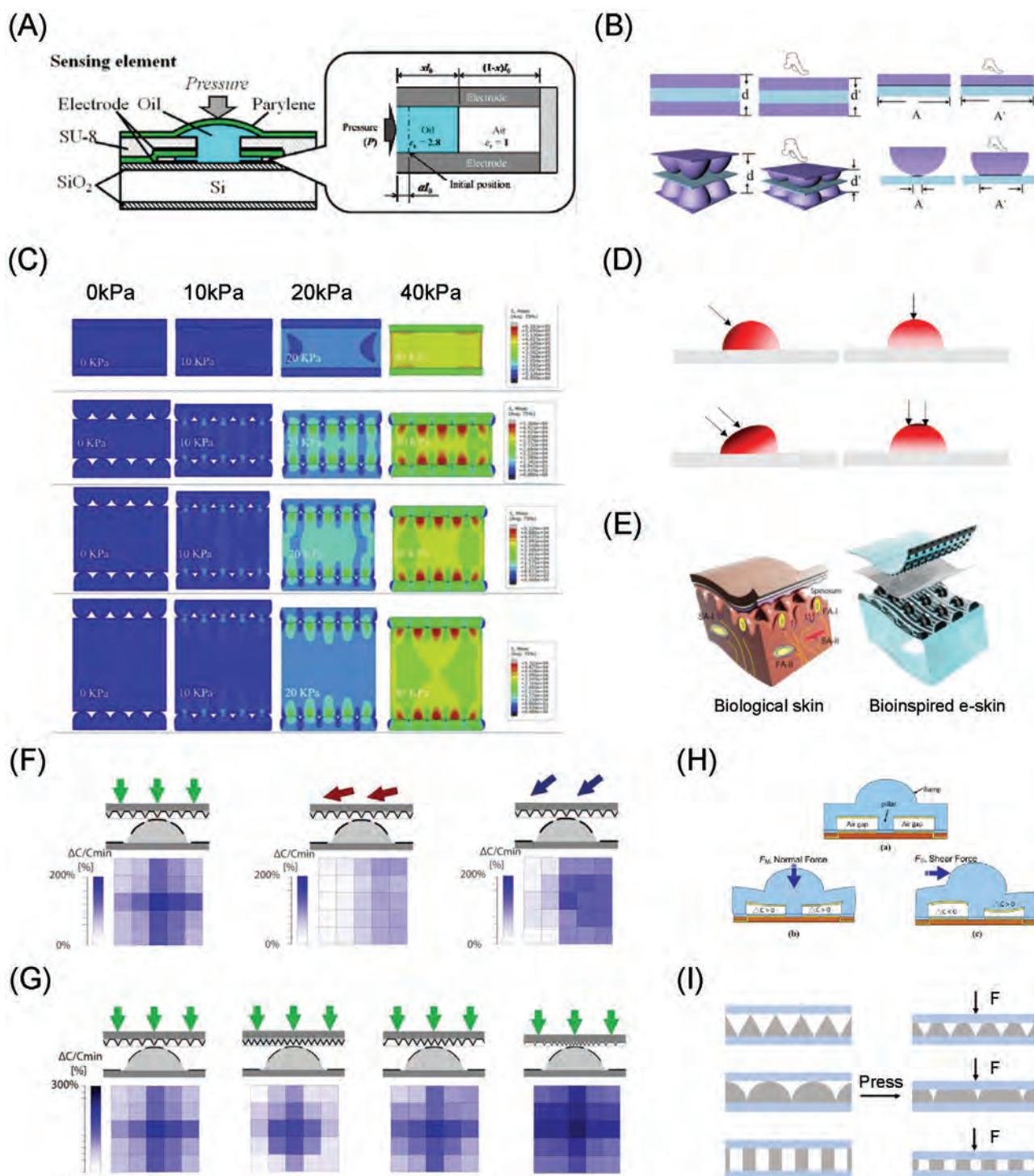


Figure 4. A) Schematic of flexible microdome pressure sensor. Adapted under the terms of the CC-BY Creative Commons Attribution 3.0 Unported license (<https://creativecommons.org/licenses/by/3.0/>).^[121] Copyright 2012, The Authors, published by MDPI. B) Schematic of distance and contact area changes when sensors without/with microstructure were loaded. C) Force analysis cloud diagram of the sensors without microdome and sensors with different dielectric layer thicknesses of 4, 7, and 10 μm , respectively. B,C) Adapted with permission.^[57] Copyright 2019, Elsevier. D) Schematic showing displacement of the structure for side and normal pressure. E) Human skin inspired E-skin. F) Schematics showing that the sensors were possible to measure and discriminate in real time normal and shear forces and forces applied in various directions. G) Measured response characteristics of E-skin, for arrays of five-by-five capacitors with orthogonal and spiral grids of pyramids. D–G) Adapted with permission.^[74] Copyright 2018, The Authors, published by AAAS. H) Schematic of a shear stress sensing element: a) without applied forces, b) with a normal force, and c) with a shear force. Reproduced under the terms of the CC-BY Creative Commons Attribution 3.0 Unported license (<https://creativecommons.org/licenses/by/3.0/>).^[122] Copyright 2010, The Authors, published by MDPI. I) Schematic of structural changes of different microstructures under the same pressure.

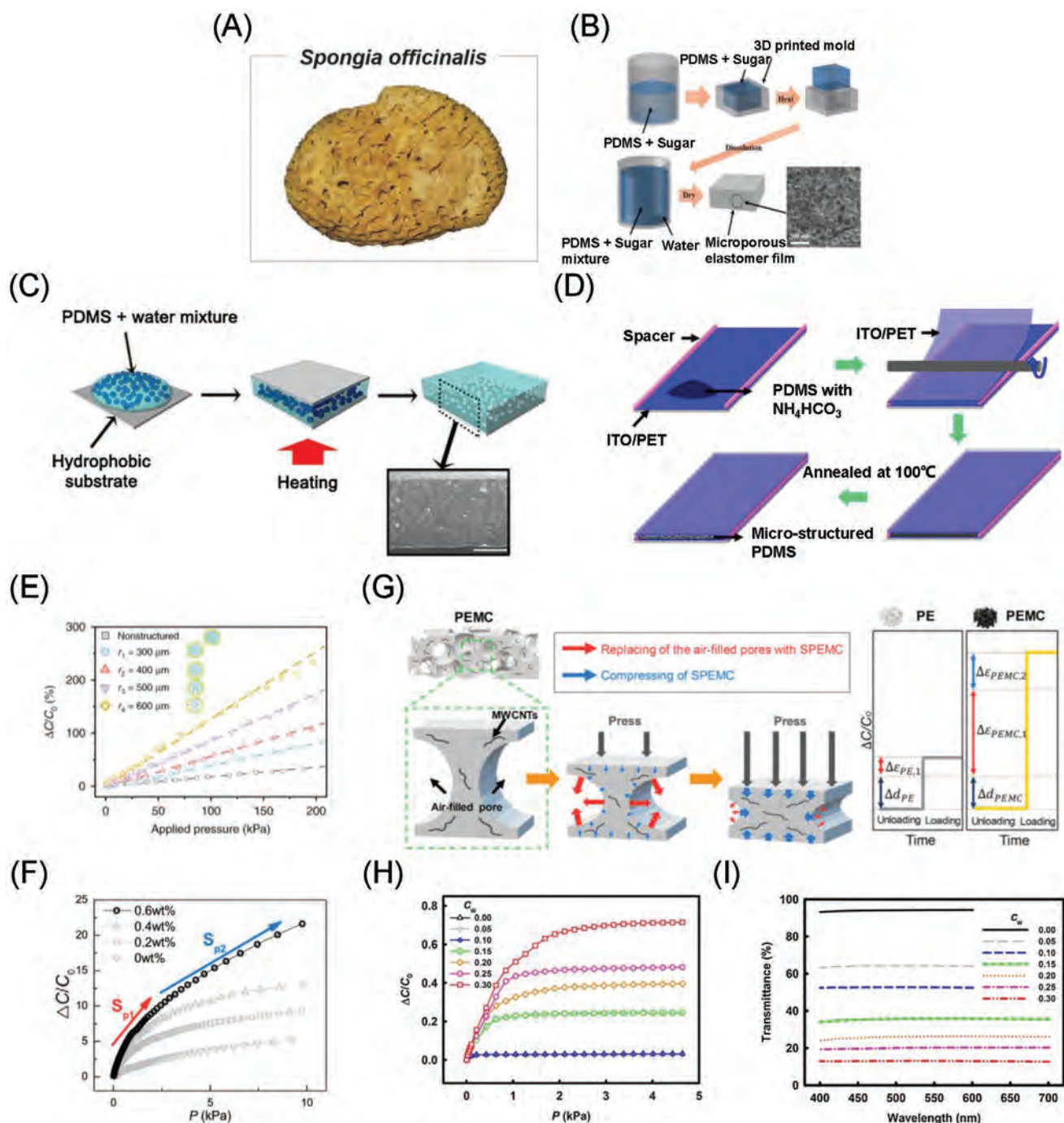


Figure 5. A) Photograph of a *Spongia officinalis*. Reproduced with permission.^[125] Copyright 2016, Wiley-VCH. B) Fabrication process of the microporous dielectric film by sugar. Adapted with permission.^[52] Copyright 2017, Elsevier. C) Fabrication process of an elastomer film with well-distributed micropores. The cross-sectional image of a portion of the porous PDMS film, observed with the SEM, was also shown. The scale bar represents 50 μm. Reproduced with permission.^[47] Copyright 2016, Elsevier. D) Schematic illustration of one-step processing of the microstructured PDMS film based on a mixture of PDMS prepolymer and its curing agent with NH_4HCO_3 and its seamless integration into the process flow for fabricating a flexible capacitive sensor. Adapted with permission.^[132] Copyright 2016, American Chemical Society. E) Capacitance–pressure curves of porous structures with different pore sizes and unstructured sensors. Reproduced under the terms of the CC-BY Creative Commons Attribution 4.0 International license (<https://creativecommons.org/licenses/by/4.0>).^[133] Copyright 2020, The Authors, published by Springer Nature. F) Hysteresis characteristics of the PEMC-based pressure sensor. G) Schematic illustration of structural change of the PEMC under compressive loading, and $\Delta C/C_0$ of the PE and the PEMC under compressive loading. F,G) Reproduced with permission.^[71] Copyright 2020, American Chemical Society. H) The $\Delta C/C_0$ as a function of the applied pressure. Note that for each weight ratio of water (c_w), three different samples were used for the measurements. I) The dependence of the transmittance of the PDMS films on c_w from 0 to 0.3 in the visible range. H,I) Reproduced with permission.^[47] Copyright 2016, Elsevier.

simple, low-cost, and environmental-friendly. The foam-like dielectric film can withstand pressure, bending, and strain. The sensor sensitivity was adjusted according to foam density (Figure 5E).^[133] Increasing the porosity can improve the sensor compressibility and expand the sensing range (Figure 5F).^[71] Park and co-workers produced a simple, economical, and highly sensitive capacitive pressure sensor based on a porous Ecoflex-multiwalled carbon nanotube composite (PEMC) material. Because of the synergistic effect of the elastomer porous structure and the CNT fillers, PEMC exhibits a high capacitance change than porous Ecoflex (PE), thus increasing sensitivity (Figure 5G).^[71] The pores in the entire volume of the composite material can reduce the volume fraction of the elastomer, thereby reducing its viscoelasticity and achieving a reversible sensor response without obvious hysteresis. Although the increase in porosity helps increase the $\Delta C/C_0$ ratio under unit load of the sensor (Figure 5H), the light becomes scattered, which can affect the transparency of the device because of the existence of holes. When the porosity increases, the light transmittance of the sensors decreases (Figure 5I).^[47]

Although an increase in the air ratio can effectively reduce the mechanical modulus and improve sensitivity,^[11,67] the current methods for preparing porous structures are usually uncontrollable. Even if the amounts of reagents or compounds used for volatilization are controlled, the uneven spatial distribution of pores greatly limits the practical application of the sensor.

2.5. Natural Plant-Based Structure

Commonly employed methods used to prepare microstructures can easily be used to realize soft imprinting of precision molds, thus obtaining accurate microstructures.^[38,107,134–136] Nonetheless, these methods usually require complicated and time-consuming mold transfer processes, which are expensive, thus making it difficult to expand production, and require hazardous chemicals. Waste disposal and environmental pollution caused by E-waste are also challenging problems.^[38,138] Compared with these microfabrication methods, natural materials have been extensively studied for their environmental protection, abundance, renewability, sustainability, degradability, and low cost.^[139,140] Natural templated sensors can also achieve the same performance without expensive and sophisticated instruments and processes and are safe and commercially promising for the development of E-skin.

Leaves or petals have rough microstructures on their surfaces, and their use as templates can significantly improve sensitivity.^[139] The microtower array structure (micrometer level) on the surface and the hydrophobic surface for easy demolding of natural lotus leaves has been widely studied.^[55,141] The lotus leaf can be reused several times as a mold, and the microcylinder does not change as fresh or dry. Zhang's group used a lotus leaf as a template to prepare a uniform microporous electrode (Figure 6A).^[84] The micropores in the PDMS/Au electrodes were rearranged via the action of the polystyrene (PS) microspheres in the dielectric layer under applied pressure (Figure 6B), to ensure that the flexible device had high sensitivity and reproducibility. Guo's group used a lotus leaf as

a template to provide a bionic micropattern (height-to-width aspect ratio of over 2) as a flexible dielectric layer on the PDMS film and covered the film by ultrathin AgNWs as the bottom electrode (Figure 6D).^[55] Both methods can significantly expand response range of the sensor (from 200 to 500 kPa,^[84] and from 6 to 8 kPa^[55]) and further improve the sensitivity (from 0.038 to 0.815 kPa⁻¹,^[84] and from 0.352 to 1.194 kPa⁻¹^[55]) (Figure 6C,E).^[55,84] In addition, Guo's group proved that the $\Delta d/d$ ratio of sparse microtowers is twice that of dense microtowers owing to the large local stress concentration and is ≈ 20 times higher than that of flat PDMS.^[55] The hierarchical structure of the micropapillae and nanofolds on the surface of red rose petals provide the necessary roughness to the pressure sensor, and the experimental results obtained by the natural hierarchical microstructure showed good linearity (Figure 6F).^[139,142] In addition, rose petals can act as dielectric layers. While pressure sensors with fresh petals have a high sensitivity (1.54 kPa⁻¹) because of the electronic double layer that is contributed by the ionic liquid in the fresh petal, sensors with dried petals have a foam-like hollow structure with high compressibility (Figure 6G).^[139] The petals can be treated using different methods according to the actual application to achieve the desired effect.

This method of using natural plants as templates is simple and effective but is inherently flawed. It completely depends on the existing natural materials and the shape, size, and spacing of their microstructures, which cannot be controlled or modified. Therefore, the prepared microstructures cannot exhibit a uniform morphology.^[39] Moreover, some templates have problems such as poor spatial distribution and uneven shape and size, which result in significant differences in the performance of different batches and difficulty in large-scale, high-resolution, and standardization production.

2.6. Discussion

The performances of pressure sensors based on microstructures are shown in Table 2. A comparison of the effects of the five common microstructures on capacitive pressure sensors is presented in Table 3. Both porous and natural plant-based structures have inherent inconsistencies. Owing to the uniformity of arrangement and distribution as well as the difference in pore-forming grains themselves, the pressure response of the sensor is diverse, which is reflected in the various effects of the applied force on the structural deformation, resulting in a large standard deviation in the preparation process. Among the existing high-sensitivity flexible pressure sensor devices, the nano- or microscale structures are the most commonly employed methods to obtain high sensitivity, especially micropyramids.^[36,102] Many researchers have constructed different microstructures through FEA, which have proved that sensors with micropyramids exhibit better performance than other microstructures because micropyramids have a high stress concentration and geometric deformation under the same pressure.^[98,99,101,143] To achieve higher sensitivity, Park's group reported an ultrahigh sensitive pressure sensor-based porous pyramid dielectric layer (Figure 7A).^[144] Combining the characteristics of the two types of microstructures, the sensors have

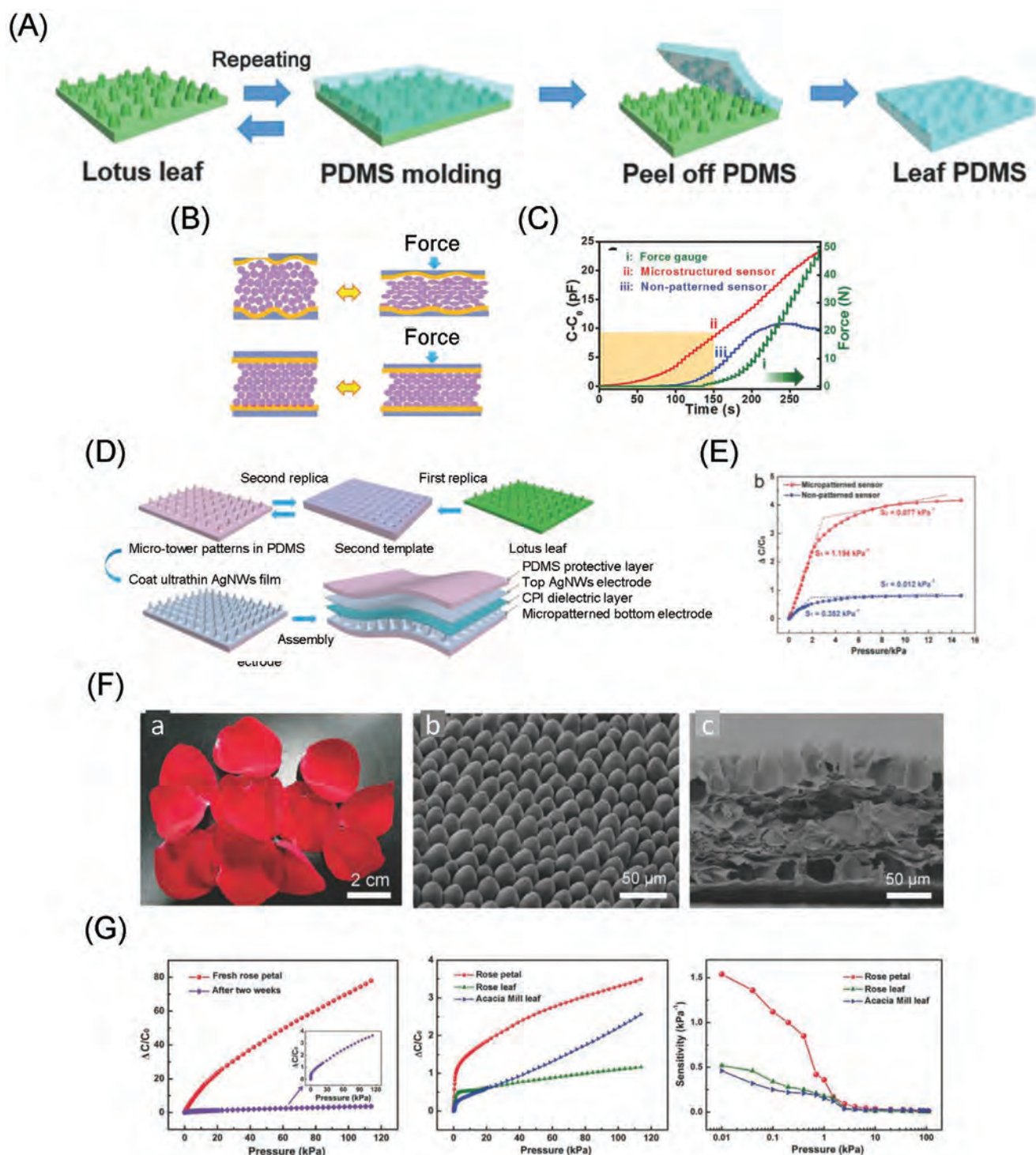





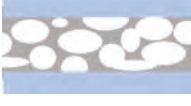
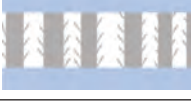
Figure 6. A) Schematic of the fabrication process for micropatterned PDMS film. B) Schematic representation for the deformation of capacitive sensors with and without micropatterned PDMS/Au electrodes. C) Real-time capacitance response curves with stepwise applied forces of microstructured sensor, nonpatterned sensor, and commercial force gauge. A–C) Adapted with permission.^[84] Copyright 2016, Wiley-VCH. D) Schematic illustration for the fabrication of micropatterned tactile sensor. E) Sensitivity of the micropatterned and nonpatterned sensor. D,E) Adapted with permission.^[55] Copyright 2017, Wiley-VCH. F) Natural materials and device structure: a) photograph of red rose petals; b) SEM image of the rose petal dried by critical point drying; c) cross-sectional SEM image of the rose petal. G) $\Delta C/C_0$ and sensitivity as a function of pressure of the E-skins based on the natural materials. F,G) Adapted with permission.^[139] Copyright 2018, Wiley-VCH.

Table 2. Summary of the performance of the pressure sensors based on microstructures.

Type		Polymer matrix	Materials	Sensitivity [kPa ⁻¹]	Response time/ recovery time [ms]	Cyclic stability	Detection limit	Pressure range [kPa]	Year	Refs.	
Micropyramid		PDMS	–	0.55	–	–	A fly	8	2010	[36]	
			Graphene	–	50/–	1000	–	5	2018	[105]	
			–	–	165/132	–	–	200	2018	[107]	
			AgNWs	0.831	30/60	10 000	1.4 Pa	10	2018	[50]	
			Pt/BOPP	3.73	21/–	10 000	0.1 Pa	100	2018	[106]	
			rGO + SWCNT	0.7	50/–	20 000		25	2018	[93]	
			Ti/Au + parylene	70.6	–	10 200 (300 Pa press) ^{a)}	1 Pa; rice: 24 mg	0.35	2020	[51]	
		TPU	SWCNT + graphene	–	–	–	–	500	2015	[76]	
		PHB/PHV	PGS	0.76 ± 0.14	–	8000	5 mg	10	2015	[109]	
		P(VDF-HFP)	EMITFSA	41.64	<20/–	5000	<400 Pa; 40 mg	50	2017	[229]	
Microneedle/ pillar		PDMS	–	0.0326 mN ⁻¹	–	20 000	–	–	2014	[54]	
			AgNWs	0.28	100	10 000	2 Pa	200	2019	[116]	
			Graphene	7.68	30/28	1000	1 mg	4	2019	[114]	
			Ag@Ni	–	49/51	9000	1.9 Pa	145	2020	[113]	
		PU	–	1.76	–	–	–	6	2012	[230]	
		PET	PVDF + AgNWs	2.94 ± 0.25	<50/–	1000	<3 Pa	7.5	2017	[82]	
		P(VDF-TrFE)	–	0.35	48/60	3000	4 Pa	25	2019	[39]	
Microdome		PDMS	–	1.67% mN ⁻¹	–	–	26 mN	0.36 N	2010	[122]	
			–	–	–	–	3 mN	0.75 N; 5.75 Pa	2012	[62]	
			–	2.8	–	–	–	3000	2014	[231]	
			–	0.2	–	5	–	120	2015	[124]	
			PVDF	30.2	25/50	100 000 (15 Pa press) ^{a)}	0.7 Pa	800	2019	[57]	
		PU	CNTs	0.19 ± 0.07	–	30 000	2.7 g	680	2018	[74]	
	Porous	Purchased + water	PDMS	TiO ₂ + SrTiO ₃ + PMN-PT	0.00324	–	–	–	40 000	2015	[232]
NH ₄ HCO ₃			–	0.26	–	3000	1 Pa	1000	2016	[132]	
Deionized water			–	1.18	150/–	–	0.2 kPa	5	2016	[47]	
Ps beads			–	0.6	40/–	10 000	2.42 Pa	14	2016	[125]	
Water-in-oil emulsion method			Carbon black	35.1	–	100	–	12	2019	[33]	
Sugar			–	0.51285	200/–	100		400	2017	[52]	
		Ecoflex	CNTs	0.601	–	10 000	0.16 Pa	40	2016	[65]	
Sugar + NaCl		Conductive fabric	0.0121	–	100	–	100	2017	[233]		
Sugar template		MWCNT	6.42	<100/–	10 000 (10 kPa press) ^{a)}	–	–	2019	[71]		
	As-prepared	PET	rGO	0.8	100/100	1000	0.24 Pa	4	2016	[129]	
	Purchased	PVDF	Ionic liquid	1.194	40/–	5000	–	120	2020	[37]	
Natural plant-based	Lotus leaf	PDMS	–	0.815	38/–	–	Hair: 18 Pa	500	2016	[84]	
			–	1.194	36/58	100 000	<0.8 Pa	10	2017	[55]	
	Calathea zebrine		[EMIM][TFSI]	54.31	29/32	5400	Leaf: 0.1 Pa	120	2018	[234]	
	Rose petals + rose leaves		–	1.54	–	5000	0.6 Pa	115	2018	[139]	
	Rose petals		–	0.055	300/280	–	–	10	2019	[142]	
	Porous-pyramid-based		–	44.5	–	5000 (400 Pa press)	0.14 Pa	35	2019	[144]	

^{a)}The contents in parentheses indicate the test conditions for cyclic stability experiments.

Table 3. Comparison of the five common microstructure influences on pressure capacitive sensors.

Type	Schematic	Advantages	Disadvantages	Summary	Challenge
Micropyramid		First proposed The best performance	Small linear range	Uniform Controllable Expensive Complex	1) Nonlinear at high pressure 2) Unstable nonstationary contact 3) Small capacitance/easily affected 4) Device thickened or opaque
Microdome		Distinguish between different forces	Greater viscosity Less deformability		
Microneedle/pillar		Larger deformation Distinguish different forces	Viscoelasticity High loss		
Microporous		Light mass Low hysteresis Fast response speed High compressibility	Uneven hole size and distribution	Uneven Uncontrolled Low-cost Simple	
Natural plant-based		Simple Green Low cost Easy to get	Difficult to standardize production		

more air phase, which results in a low modulus, large change in the dielectric constant under pressure, and consequently, a high sensitivity (44.5 kPa⁻¹).

Although these uniform microstructures can improve the sensitivity, they exhibit nonlinearity in the range of higher pressures.^[36,58,65,84,100,108–112] Under specified conditions, linearity is defined as the percentage of the maximum deviation and the full-scale output value between the sensor's static calibration curve (the actual curve) and the fitted curve. A high degree of nonlinearity affects the judgment of the object deformation degree and augments the uncertainty between the output and input values. From a mechanical viewpoint, the sharp parts of the microstructures allow it to be easily compressed under external forces. However, the microstructures are gradually flattened as the load increases, and their deformability reduces as the elastic modulus increases. The proportion of the polymer matrix in the capacitive device and the contact area between the microstructures and opposite surfaces tend to be saturated. Thus, the corresponding curve of the capacitance value and load has a higher sensitivity in the low-pressure range and nonlinearity in the high-pressure range. This phenomenon complicates the relationship between capacitance and pressure^[105] and deteriorates the reproducibility and reliability of the sensor under high input loads.^[60] By analyzing the pressure-response curves of different microstructure sensors, Miller and Bao found that the pressure response produced by nonuniform, polydisperse structures is more linear and has higher sensitivity under high pressures.^[124] When the dielectric contains nonuniform microstructures, only the higher microstructures are compressed initially, and then, the other smaller microstructures will begin to be compressed with an increase in load. This structure with a nonuniform distribution has higher sensitivity and better linearity than a single uniform microstructured dielectric when compressed at higher pressures.^[145] However, the effects of

various methods to improve linearity are not ideal, and the definition of the high-pressure range varies for each study. Therefore, the performances of sensors developed in different studies cannot be accurately compared due to the lack of standardized parameters.

The presence of air in the microstructure is also an important factor that affects the stability of the sensor. When a small force is applied to the device, the gas phase is easily deformed, thus improving the sensitivity of the sensor.^[62,96,97] However, this design has inherent defects, and the air in the dielectric layer can cause unstable baselines and unreproducible sensitivity.^[40,71,84] Luo et al. tightly combined the connection part of the tilted micropillars array and the corresponding electrode layer to eliminate the existence of an unstable air phase (Figure 7C).^[146] The tilt of the micropillar was used to replace the compression deformation under load so that the sensor exhibited high deformation (Figure 7D), a large capacitance change (Figure 7E), high stability, mechanical robustness, and a reliable capacitive response.^[146] Because of these characteristics, the device does not need to be repaired or replaced after mechanical damage in normal use; however, the problem of nonlinearity still exists.

Because most microstructures are on the micrometer scale, which causes a certain amount of light scattering, the device becomes thicker or opaque (Figure 7F,G)^[37,100,147,148] and affects the practical application of the sensor. In addition, the capacitance value of the electromagnetic interference in circuits and the environment (or human body) usually reaches the pF level.^[106,149] In the presence of air in the microstructure, which reduces the initial capacitance, sensors are easily disturbed by external noise sources and exhibit large discrete errors.^[37,70,150] This problem harms the measurement accuracy and repeatability, which limits its application in weak signal detection and high-density integration.^[39,81,151]

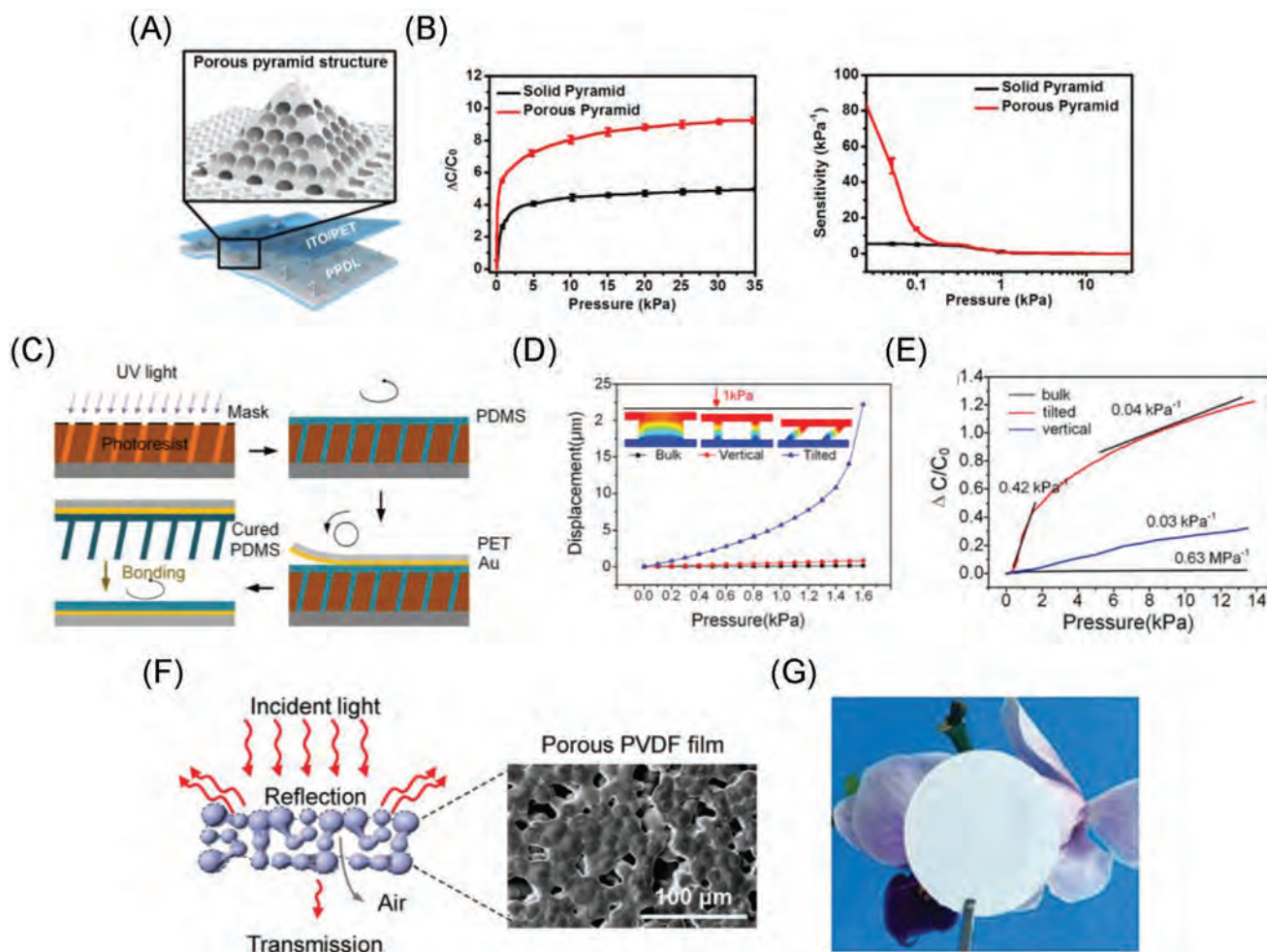


Figure 7. A) Schematic and B) capacitance and sensitivity versus pressure of capacitive pressure sensor based on porous pyramid dielectric layer. A,B) Reproduced with permission.^[144] Copyright 2019, American Chemical Society. C) Schematic diagram of the capacitive pressure sensor fabrication process. D) Electrode displacement versus pressure curves of different structures, obtained by FEA. E) Pressure–response curves of the capacitive pressure sensors for dielectric layers with bulk film, vertical micropillar array, and tilted micropillar array. C–E) Reproduced with permission.^[146] Copyright 2019, American Chemical Society. F) Schematic diagram for the opaque mechanism and SEM images of the porous PVDF film (inset). G) Photograph of the porous PVDF film. F,G) Adapted under the terms of the CC-BY Creative Commons Attribution 4.0 International license (<https://creativecommons.org/licenses/by/4.0>).^[37] Copyright 2020, The Authors, published by Wiley-VCH.

3. Stretchable Strain Sensors

Although high sensitivity is an important sensing performance parameter, most pressure sensors can only bend in a single direction and do not allow multiple repetitions of double-curvature bending and plane shear.^[152] Comparatively, stretchable sensors can better attach to surfaces similar to the human skin, which is of more practical value.^[10,153] Because the human body comprises numerous nonflat surfaces and has a fine topology, it is difficult to use real-time diagnosis to closely attach the sensor to such irregular and rough structures.^[38] To solve this problem, the sensor circuit must be stretchable and flexible, compatible with the compliance of natural biological tissues, and potentially incorporated into wearable technology and E-skin of soft robots. Compared with traditional rigid electronic components, these circuit elements maintain their sensing function even when stretched to several times their natural length.^[68]

The deformation of stretchable dielectrics under tension is mainly affected by the Poisson's ratio of the dielectric and flexible substrate.^[89] Owing to the Poisson effect, longitudinal stretching of the capacitive sensor causes an increase in the length, whereas its width and thickness decrease (Figure 8A). The linear mechanics of this process can be described as follows^[68,71,86–89]

$$\frac{\Delta l}{l} = \epsilon_x \quad (5)$$

$$\epsilon_y = \epsilon_z = -\nu \epsilon_x \quad (6)$$

$$\begin{aligned} l_{\text{stretch}} &= l + \Delta l = l + \epsilon_x l = l(1 + \epsilon_x) \\ w_{\text{stretch}} &= w - \Delta w = w - \nu \epsilon_x w = w(1 - \nu \epsilon_x) \\ d_{\text{stretch}} &= d - \Delta d = d - \nu \epsilon_x d = d(1 - \nu \epsilon_x) \end{aligned} \quad (7)$$

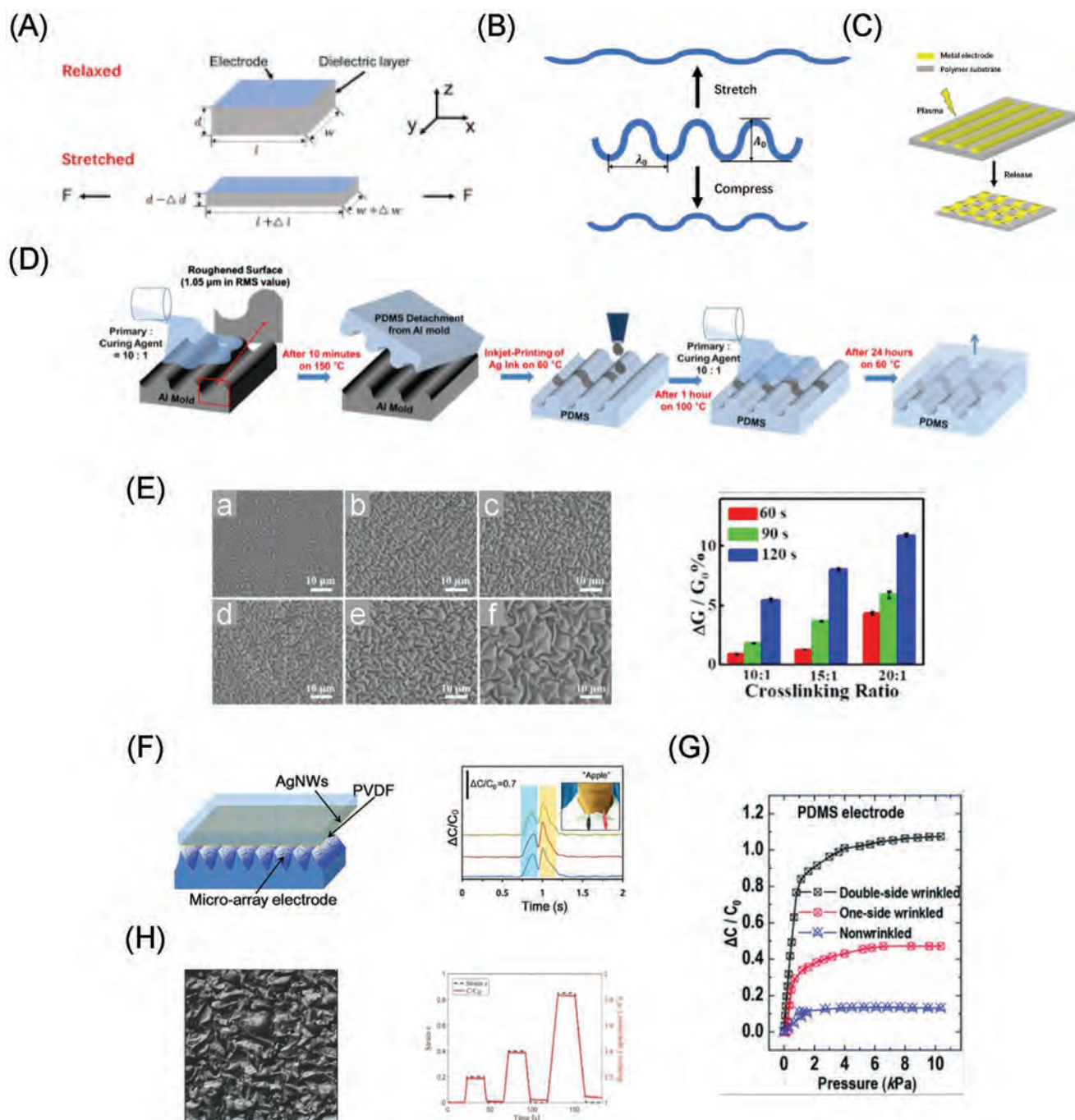


Figure 8. A) Response mechanism of the parallel plate capacitors under tension. B) Wave structure response to tension and compression. C) Schematic illustration of the process for fabricating parallel metal electrode on a polymer substrate. D) Process flow of the inkjet-printed stretchable Ag electrode. A–D) Adapted with permission.^[156] Copyright 2011, American Institute of Physics. E) SEM images of 2D Ag microwrinkles on flat PDMS surface prepared via different conditions: varying PDMS crosslinking ratio as: a) 10:1, b) 15:1, and c) 20:1, under the same electroless deposition time (60 s); varying electroless deposition time as: d) 60 s, e) 90 s, and f) 120 s, with the use of PDMS at a given crosslinking ratio (20:1), and pressure-response curves of sandwiched Ag wrinkle sensors with the different combinations of PDMS crosslinking ratio and Ag deposition time. E) Adapted with permission.^[157] Copyright 2016, American Chemical Society. F) Schematic of the capacitive pressure sensor, and real-time response of the flexible pressure sensor to voice vibrations. Adapted with permission.^[82] Copyright 2017, American Chemical Society. G) The relative capacitance change versus the normal pressure as a function of the wrinkled structures of the Ecoflex template, using PMDS electrodes coated with Au. Adapted under the terms of the CC-BY Creative Commons Attribution 3.0 Unported license (<https://creativecommons.org/licenses/by/3.0/>).^[158] Copyright 2017, Royal Society of Chemistry. H) SEM image of electrode surface, and capacitance change as a function of time for sensors subjected to step deformation at different strain levels. Adapted with permission.^[159] Copyright 2017, Wiley-VCH.

$$\begin{aligned} C_{\text{stretch}} &= k_0 k_{\text{matrix}} \left(\frac{l_{\text{stretch}} w_{\text{stretch}}}{d_{\text{stretch}}} \right) \\ &= k_0 k_{\text{matrix}} \left(\frac{l(1+\varepsilon_x)w(1-\nu\varepsilon_x)}{d(1-\nu\varepsilon_x)} \right) \\ &= k_0 k_{\text{matrix}} \left(\frac{lw}{d} \right) (1+\varepsilon_x) \\ &= C_0 (1+\varepsilon_x) \end{aligned} \quad (8)$$

where l , w , and d are the length, width, and thickness of the sensor, respectively, and ε_x , ε_y , and ε_z represent the strains applied on the x , y , and z axes, respectively; l_{stretch} , w_{stretch} , and d_{stretch} are the length, width, and thickness of the sensor after applying strain, respectively, ν is the Poisson's ratio of the flexible substrate, k_0 is the vacuum dielectric constant, and k_{matrix} is the relative dielectric constant of the flexible substrate. The results indicate that when strain ε_x occurs, the stretched capacitance C_{stretch} is $(1+\varepsilon_x)$ times that of the initial capacitance C_0 . Therefore, the structure should be changed to achieve high stretchability and deformity for high sensitivity.

Wearable sensors must measure high levels of strain (e.g., 50% or more) to detect human posture or movement.^[154] Most polymer elastomers have a certain degree of stretchability; however, traditional metal electrodes cannot withstand large tensile deformations and cannot generally be stretched to exceed a strain level of 1–2%.^[155] Hence, long-distance propagation of cracks cause electrode discontinuities in the metal deposition area, which reduces the conductive paths and the overlapped conductive electrode areas, thereby adversely affecting the linearity and sensitivity of the sensor.^[159] Therefore, most studies have focused on geometric modification of the electrode layer to allow the deposited metal to exhibit stretchability under high strain.^[156,160–165] However, although there is strong adhesion between the hard electrode layer and the soft dielectric layer, excessive deformation will cause the electrode layer to crack and lose conductivity, thereby affecting the accuracy and service life of the sensor,^[76,166] because of which the sensors cannot meet requirements of stretchable flexible electronic products. Therefore, introducing microstructured metal electrodes is important to improve the stretchability of sensors.

3.1. Wave/Wrinkle/Buckling Structure

Wrinkles are special structures that imitate the texture of human skin or fabric surfaces,^[167,168] and can be applied to both pressure and strain sensing (Figure 8B). At present, numerous electrodes are fabricated using hard metal or carbon materials with a polymer matrix; however, their conductivity decreases as the applied strain increases, which affects their performance under tensile conditions.^[169] The wrinkle structure can endow hard materials such as metals or semiconductors with the ability to withstand deformation. The manufacturing methods for wrinkles are low-cost and uncomplicated.^[108] Wrinkles are generally achieved by depositing a film or metal electrode with a high modulus on a prestrained elastic substrate, and the system relaxes after being released to form a sinusoidal corrugated structure (Figure 8C).^[9,164,170–172] Furthermore, results similar to wrinkles can be obtained without prestrain using a wave-shaped elastic substrate before film deposition

(Figure 8D).^[156,173–175] To produce an ideal wrinkle structure, the polymer surface is usually treated with ultraviolet/ozone (UV/O₃) or plasma.^[108] PDMS surfaces are selectively activated by UV/O₃ exposure or oxygen plasma treatment, which irreversibly forms strong siloxane bonds (–O–Si–O–) with other film surfaces,^[176,177] whereas inert areas (unexposed areas) retain the unmodified surfaces that interact through only weak van der Waals forces with other surfaces.^[178,179] The wrinkle structure is similar to a sinusoidal curve, and the nonlinear analysis of its initial buckling geometry is as follows^[172,180,181]

$$\begin{aligned} \lambda_0 &= \frac{\pi h_{\text{electrode}}}{\sqrt{\varepsilon_c}} \\ A_0 &= h_{\text{electrode}} \sqrt{\frac{\varepsilon_{\text{pre}}}{\varepsilon_c} - 1} \end{aligned} \quad (9)$$

where λ_0 is the initial wavelength, A_0 is the initial amplitude, $h_{\text{electrode}}$ is the thickness of the electrode layer, ε_{pre} is the prestrain applied to the flexible polymer substrate, $\varepsilon_c = 0.52 \left[\frac{E_{\text{sub}}(1-\nu_{\text{electrode}}^2)}{E_{\text{electrode}}(1-\nu_{\text{sub}}^2)} \right]^{2/3}$ represents the critical buckling strain, E_{sub} is the Young's modulus of the flexible substrate, $E_{\text{electrode}}$ is the Young's modulus of the electrode, $\nu_{\text{electrode}}$ is the Poisson's ratio of the electrode, and ν_{sub} is the Poisson's ratio of the flexible substrate. As can be seen from Equation (9), both λ_0 and A_0 in the initial state linearly depend on $h_{\text{electrode}}$; however, only A_0 is related to ε_{pre} , whereas λ_0 is independent of ε_{pre} .

When $\varepsilon_{\text{pre}} > \varepsilon_c$, the wavelength λ and amplitude A of the buckling structure change with ε_{pre} ^[172,180,181]

$$\begin{aligned} \lambda &= \frac{\lambda_0}{(1+\varepsilon_{\text{pre}})(1+\xi)^{1/3}} \\ A &\approx \frac{A_0}{\sqrt{1+\varepsilon_{\text{pre}}}(1+\xi)^{1/3}} \end{aligned} \quad (10)$$

where $\frac{\lambda_0}{1+\varepsilon_{\text{pre}}}$ and $\frac{A_0}{\sqrt{1+\varepsilon_{\text{pre}}}}$ represent changes in the expected wavelength and amplitude based on the mechanics of accordion bellows, $\xi = 5\varepsilon_{\text{pre}}(1+\varepsilon_{\text{pre}})/32$, which depends only on ε_{pre} .

When the buckling structure is subjected to an external force $\varepsilon_{\text{applied}}$, the wavelength and amplitude of the buckling structure change with $\varepsilon_{\text{applied}}$ ^[172,180,181]

$$\begin{aligned} \lambda &= \frac{\lambda_0 (1+\varepsilon_{\text{applied}})}{(1+\varepsilon_{\text{pre}})(1+\varepsilon_{\text{applied}}+\zeta)^{1/3}} \\ A &\approx h_{\text{electrode}} \frac{\sqrt{\frac{\varepsilon_{\text{pre}}-\varepsilon_{\text{applied}}}{\varepsilon_c} - 1}}{\sqrt{1+\varepsilon_{\text{pre}}}(1+\varepsilon_{\text{applied}}+\zeta)^{1/3}} \end{aligned} \quad (11)$$

where $\zeta = 5(\varepsilon_{\text{pre}} - \varepsilon_{\text{applied}})(1+\varepsilon_{\text{pre}})/32$, which depends on both ε_{pre} and $\varepsilon_{\text{applied}}$.

Gao et al. adjusted the wavelength and amplitude of wrinkles by adjusting the crosslinking ratio of the polymer substrate or electrode deposition time, thereby adjusting the sensitivity and sensing range of the sensor (Figure 8E).^[157] The polymer crosslinking ratio can also adjust the viscoelasticity of the matrix to form a relatively strong adhesion with the electrode

layers, thereby ensuring good structural stability under repeated loads.^[169] However, the electrode layer inevitably cracks because of the mismatch in the elastic modulus between the hard electrode layer and the soft dielectric layer,^[76,166] thus shortening the service life of the sensor.

For pressure sensing, the air part in the wrinkles can reduce the effective mechanical modulus,^[11] which will improve sensor sensitivity.^[182] Zhu's group processed a prestretched PDMS film through a dry low-pressure air plasma to produce a flexible sensor, which exhibited good performance in the noncontact mode, such as in the process of detecting sound vibration and airflow (Figure 8F).^[82] The plasma treatment method is uncomplicated, efficient, and convenient to operate; however, while excessive corrosion or secondary pollution may occur on the surface of the material.^[82,108,182,183] Chen et al. used a sodium hydroxide (NaOH)-treated crosslinked poly(methyl methacrylate) (PMMA) film as the separation layer to prepare an ultrathin and ultralight (<60 g m⁻²) solution-based layering polymer film. The AgNW/PMMA film was attached to prestretched PDMS film, and then, the PDMS film was released to its initial state to form a wrinkle structure.^[184] However, NaOH is strongly alkaline, highly corrosive, and using it in the preparation process is a dangerous task, which pollutes the environment. Baek et al. prepared a wrinkled Ecoflex film by simple stretching and releasing to produce a wrinkled surface microstructure with a size of tens of micrometers.^[158] The effect of the surface microstructure of the wrinkled film on the sensor performance was systematically studied by comparing the unwrinkled film, single-sided wrinkle film, and double-sided wrinkle film. The double-sided wrinkled pressure sensor can effectively improve the sensitivity of the sensor and speed up the response and release time compared with unwrinkled film (Figure 8G).^[158]

For strain sensing, the wrinkled structure can absorb the main tensile strain when the flexible substrate is released^[185] and can continuously transform the tensile strain into bending, thereby adapting to external deformation and effectively improving the stretchability of hard devices^[153] without mechanical damage.^[180] Using the anisotropic characteristics of the wrinkles and buckling structures, strains in different directions can be distinguished, thus allowing the sensors to accurately monitor the motion and surface state of target objects.^[186,187] Arab Hassani et al. prestretched a double-sided adhesive acrylic elastomer to 200%, and then released it and added it to the polyimide (PI) substrate to obtain a sensor with a wrinkled structure to monitor force and tension.^[188] Atalay et al. created a wrinkled structure by a combination of direct-write laser raster and biaxial stretching, which can greatly improve the stretchability of the soft sensor and conductive electrode, with an electrode conductivity of the electrode up to 250% and a linear output of capacitance sensor up to 85% (Figure 8H).^[159]

The performances of the sensors based on the wrinkle structure are shown in Table 4. Methods for fabricating microstructured molds using spontaneous buckling of polymer films are simple, low-cost, and useful for most flexible devices converted to stretch.^[153] However, the mechanical properties of metal materials limit further improvement of their stretchability. Moreover, their microstructures are irregular and uncontrollable. The pressure sensor has poor stability and reliability for different batches of samples.^[82] In addition, the stretch–release

process may lead to the appearance of rough surfaces, which is not ideal for practical applications.^[153] Texture-based sensors have poor elasticity in the operating range, have a low baseline capacitance, and are susceptible to mechanical friction with high hysteresis.^[70]

3.2. Serpentine Structure

Although numerous studies on wrinkles have been conducted, stretchability is only allowed in the direction of the fold, which leads to poor flexibility or little stretchability in other directions.^[153] The fractal-inspired serpentine structure allows biaxial strain and even distortion that extends out of the device plane by selective attachment to the elastic substrate.^[180,189–193] Furthermore, nonstretchable squares can be repeatedly cut and subdivided into smaller squares. After multiple subdivisions, the structure becomes more complicated, the scalability becomes stronger, and the stretchability is improved (Figure 9A).^[194] Using a similar method, the serpentine structure buckles due to the change in amplitude or wavelength when the applied strain reaches a critical value (Figure 9B).^[195,196] Without stress concentration, the structure can prevent the material from delamination or cracking,^[197] ensuring that the strain on the metal electrodes is maintained below their elastic limit. Therefore, the electrode maintains a conductive path during the deformation process and achieves a greater range of stretchability.^[169,191,198,199]

A serpentine structure can be considered to be a simple structure composed of two straight lines with a length of l_1 and a semicircle with a diameter of l_2 (width w and thickness t).^[161,200,201] Through modeling and experiments, the deformation process of the serpentine structure can be divided into three stages: 1) the wrinkling stage ($t \leq 2 \mu\text{m}$, $\frac{t}{w} < \left(\frac{3\overline{E}_{\text{sub}}}{\overline{E}_{\text{electrode}}}\right)^{\frac{1}{3}} \frac{l}{2\pi w}$): the elastic stretchability first increases and then decreases as t increases; 2) the buckling stage ($2\text{--}50 \mu\text{m}$, $\left(\frac{3\overline{E}_{\text{sub}}}{\overline{E}_{\text{electrode}}}\right)^{\frac{1}{3}} \frac{l}{2\pi w} < \frac{t}{w} < 1$): the elastic stretchability monotonically increases to saturation with t (when $t = 45 \mu\text{m}$, elastic stretchability is 100%); 3) the shearing stage ($t > 45 \mu\text{m}$, $1 < \frac{t}{w}$): the elastic stretchability is independent of t (Figure 9C).^[161] In the above equations, $\overline{E}_{\text{sub}}$ and $\overline{E}_{\text{electrode}}$ are the plane-strain modulus of the flexible substrate and the electrode, respectively, and usually $\overline{E}_{\text{sub}} \ll \overline{E}_{\text{electrode}}$.^[161,200] The results suggest that in addition to the influence of the cross-sectional aspect ratio t/w , the elastic stretchability of the serpentine structure also increases when the yield strain and serpentine spacing (l/w) increase.^[201]

In addition to adjusting the parameters to enhance ductility (Figure 9D), the fractal design of serpentine geometry also exhibits response characteristics of orientation and spatial customization.^[202] The rich fractal graphics can be used as a space-filled structure with generalizable design rules, which can be promoted and installed on the skin as a wearable device. Kim's group designed a sensor array with a serpentine structure so that its stretching could be adjusted according to the dynamic mechanical characteristics of the target skin segment (Figure 9E,F).^[203] Pan's group applied Ag serpentine electrodes

Table 4. Summary of the sensors based on wrinkles structure.

Type	Polymer matrix	Materials	Max strain [%]	Sensitivity [kPa^{-1}]	Response time/recovery time [ms]	Cyclic stability	Detection limit	Pressure range [kPa]	Remarks	Year	Refs.
UV/O ₃ treatment + prestretched PDMS	PDMS + PMMA or PVP	AgNWs	—	>3.8	<150/—	1500 (1.5 kPa press) ^{a)} 5000 (bend) ^{a)}	40 mg/15 Pa	5	Sense the pressure distribution of each finger when grabbing an object	2012	[108]
Si substrate patterned with rectangular AgNW films	PDMS	AgNWs	50	—	—	4 (20% strain) ^{a)}	—	—	—	2012	[205]
Plasma treatment of dry low-pressure air + prestretched PDMS		PVDF + AgNWs	—	2.94 ± 0.25	<50/—	1000	<3 Pa	7.5	Wrinkles + microhairs	2017	[82]
Plasma		—	—	2.04 ± 0.16	<100/—	—	<7 Pa/70 mg	9	—	2018	[183]
Plasma treatment under low-pressure air + prestretched PDMS		BaTiO ₃ + PVDF	—	4.9	<50/—	5000	<1.7 Pa	10	—	2019	[235]
UV/O ₃ exposure + prestretched PDMS		Ti/Au-PET	—	14.268	50/<0.2 s	10 000	1.5 Pa	40	Respiratory monitoring and vocalization recognition	2019	[11]
UV/O ₃ radiation + prestretched Ecoflex	Ecoflex	Au-coated electrode	—	0.013	578/782	50 (press) ^{a)}	150 mg	10	Double-side wrinkled template	2017	[158]
—	Block copolymer	Photonic crystal	100	—	80/78	5000 (50% strain) ^{a)}	—	—	The strain-responsive structural color	2018	[236]
Prestretched PS	PS	Au	200	0.148	<10/<17	(Up to 10 Hz) ^{a)}	1 N	600	—	2019	[182]
Prestretched PDMS	PDMS + PMMA	AgNWs + PEDOT:PSS	40	2.76	—	3000 (bend) ^{a)} 3000 (20% strain) ^{a)}	50 Pa; 12 mg	1	Controlling all actions of a shooting computer game with only three fingers	2019	[184]
Biaxial prestretched acrylic tape (3M VHB 4905)	PVDF-HFP	Silver flakes + PVDF nanofibers	800	—	—	5000 (50% strain) ^{a)}	—	—	Wrinkles + woven fibers	2019	[221]

^{a)}The contents in parentheses indicate the test conditions for cyclic stability experiments.

based on PET to prepare of a stretchable flexible sensor, realizing the static and dynamic mapping of large-scale spatial contact/pressure/strain distribution (Figure 9G).^[204] From 30°, 45°, 60° to 90°, the change in capacitance increased linearly with an increase in the arm bending angle. Liquid metals are promising materials for strain sensors because they can withstand large deformations while maintaining electrical conductivity. Fassler and Majidi injected a liquid alloy into an Ecoflex elastomer through a 3D printed mold to create microchannels and prepared a square-wave capacitor comprising two serpentine electrodes that shared the main axis. When the sensor was stretched along this major axis, the capacitance of the square wave capacitor changed along with the extension of the electrode (Figure 9H).^[68] In addition to hyperelastic strain sensing, soft capacitors and inductors can also serve as circuit components for wireless communication and analog filtering, as well as in RLC circuits for high-band pass filtering and radio frequency oscillators.

Although the serpentine structure can provide a metal electrode sensor with excellent stretchability, the preparation of

a serpentine structure requires expensive lithography and vacuum metal evaporation,^[205] which greatly increases the manufacturing cost. The snake-like electrode reduces the contact area of the conductive part, thereby increasing the impedance between the electrode and skin and reducing capacitance.^[1,206,207] A smaller capacitance results in a lower SNR,^[70,106,150] which is susceptible to interference from external noise caused by circuits and the environment (or human body), thus affecting the reliability of measurement.^[37,149]

3.3. Mesh Structure

3.3.1. 2D Mesh

Numerous electrodes are composed of relatively hard metals (or carbon materials) and polymer matrices; however, their conductivity decreases with an increase in the applied strain, which affects their performance under tensile conditions.^[169]

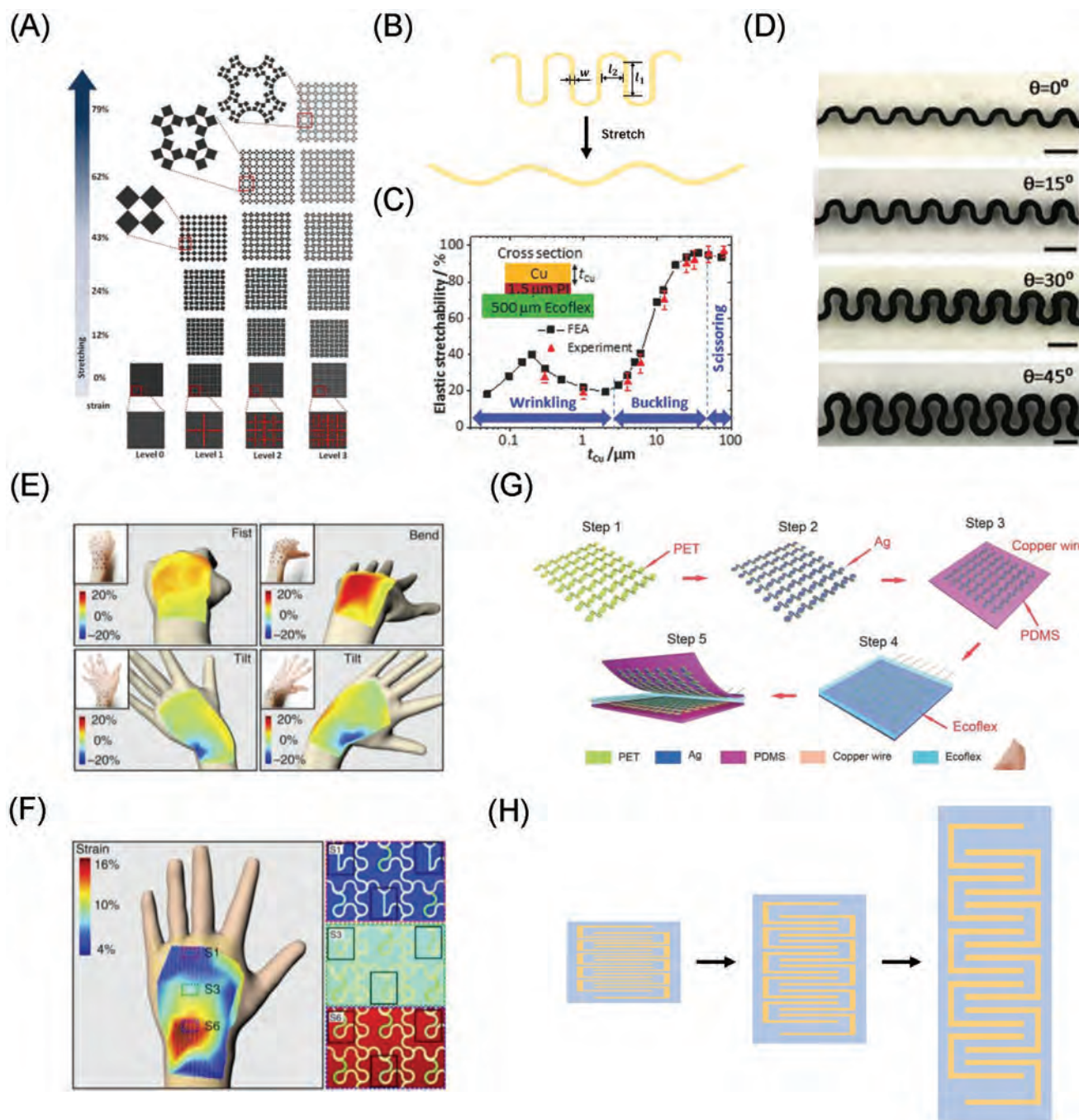


Figure 9. A) Finite element calculations for finite size hinges in silicone rubber. The cuts can be combined in a multilevel hierarchy. Reproduced with permission.^[194] Copyright 2014, The Authors, published by National Academy of Sciences USA. B) Schematics showing the stretching process of the serpentine design. C) Experimental fatigue measurement and FEA study of the dependence of the elastic stretchability on the thickness of Cu interconnects. B,C) Reproduced with permission.^[161] Copyright 2017, Wiley-VCH. D) Cross-sectional photographs of the 3D printed wavy electrodes with different joining angles. Scale bar: 5 mm. Adapted with permission.^[202] Copyright 2017, Wiley-VCH. E) Regional strain maps of the skin, calculated using positional information acquired by motion-capture system for four different motions: clenching fist, front bending, tilting left, and right. F) Map of maximum stretching range for the entire area acquired by combining the data from (E), and corresponding arrangement of site-specifically designed single crystalline silicon nanoribbon strain gauge. E,F) Reproduced with permission.^[203] Copyright 2014, Springer Nature. G) Schematic illustration of the device fabrication process. Reproduced with permission.^[204] Copyright 2015, Wiley-VCH. H) A square wave sample at different strain is shown.

By aligning the serpentine electrodes orthogonally, a 2D mesh structure can be formed, which further increases the ductility

(Figure 10A).^[197,208] If a metal film is designed in a network structure, stretchability will be improved.

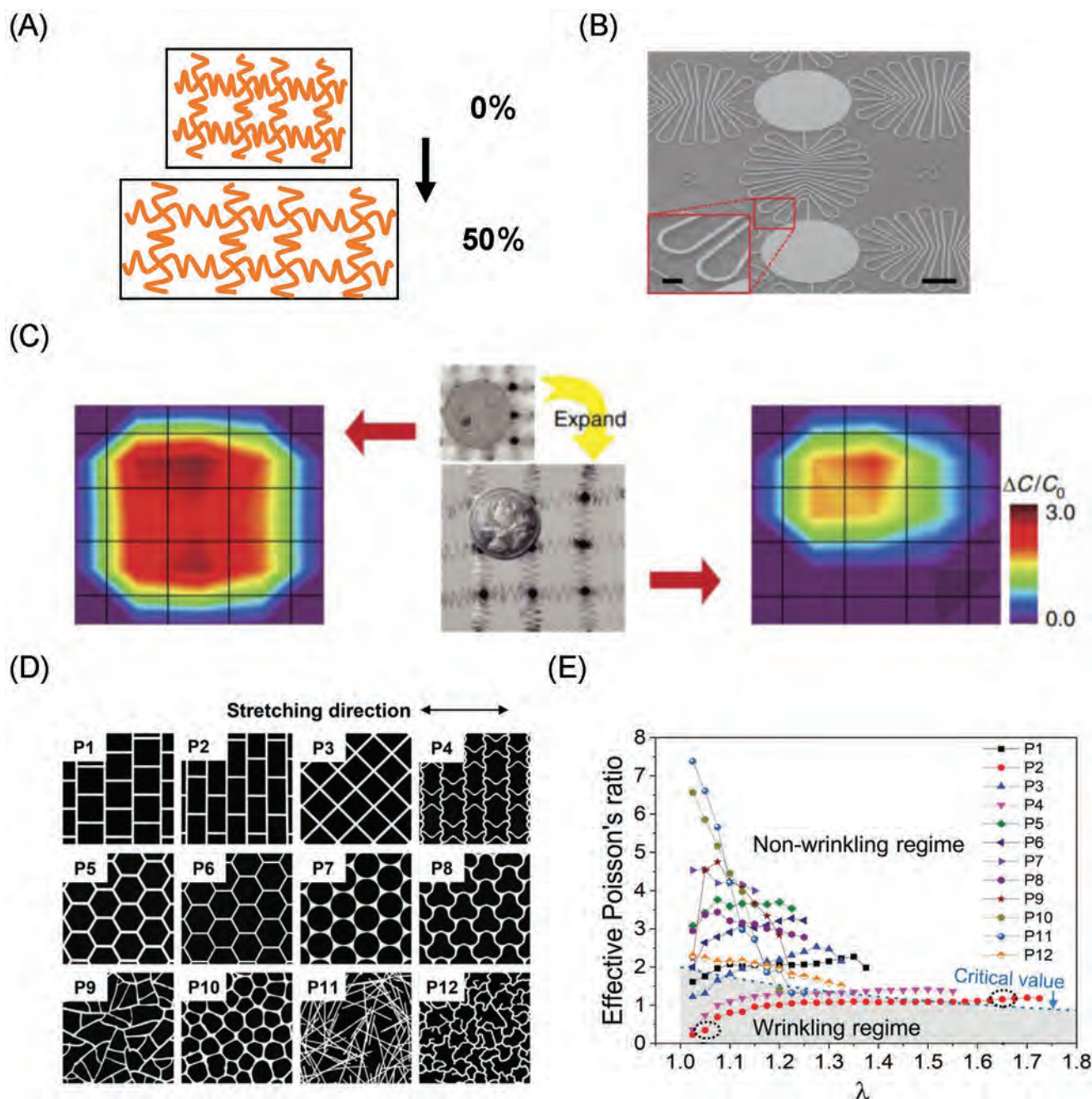


Figure 10. A) Schematic of stretched memory on PDMS. B) Tilted SEM image of the polyimide network (scale bar: 500 μm); the inset is a higher-resolution SEM image of a meandering interconnect (scale bar: 50 μm). C) Pressure mapping before and after the 300% expansion of an SCM; the position of the pressure load is also identified after expansion. A–C) Adapted under the terms of the CC-BY Creative Commons Attribution 4.0 International license (<https://creativecommons.org/licenses/by/4.0>).^[209] Copyright 2018, The Authors, published by Springer Nature. D) Structures with different shapes are labeled P1–P12. E) Effective Poisson's ratio curves under tensile strain corresponding to different structures in (D). D, E) Adapted with permission.^[166] Copyright 2019, Wiley-VCH.

Inspired by human skin, Wang's group designed a highly stretchable metal-matrix network. A network structure has 100 winding wires that connect the sensing nodes to achieve multifunctional use of scalable sensing performance (Figure 10B).^[209] The specific scalable sensor unit was assembled on a structured PI network for 3D integration, with an adjustable sensing range (sensitivity up to 22.4 MPa^{-1}) and large area expansion

capability (Figure 10C).^[209] Ying et al. used a silicon nanofilm (SiNM) diode-multiplexed electrode array for electrical stimulation. A SiNM pressure gauge was used for high-sensitivity strain monitoring, and an elastic capacitor was used for tactile sensing. The importance of nanogeometry in achieving the required mechanical properties was demonstrated via mechanical analysis and FEA.^[201] In addition to using serpentine

network structures, other shapes can also be used to form more complex network structures to allow the sensors to withstand more complex deformations, such as rotation or twisting.^[10,210] Wang et al. designed 2D mesh structures with 12 different shapes through laser cutting, including common regular and irregular shapes (Figure 10D).^[166] By comparing and analyzing the changes in the effective Poisson's ratio and wrinkling state of different structures with increasing strain, they found that the commonly used structures (P1–P4) were wrinkled within a larger prestrain range, whereas the AgNW imitating network film (P11) and the AuNM film (P12) designed in the reference (Figure 10D)^[166] were in an unwrinkled state within a larger prestrain range (Figure 10E). This conclusion provides good guidance for designing flexible transparent electrodes.

A metal penetration network is an ideal stretchable electrode structure. However, it is very difficult to construct a 2D mesh structure.^[197] Moreover, the network structure has problems associated with small electrode areas and small capacitance, such as the serpentine structure. Problems such as those associated with smaller sensing capacitors require sophisticated devices for measurement^[106] and are susceptible to interference from external noise or parasitic capacitance (electromagnetic interference in circuits and ambient noise are usually up to the pF level).^[37,38,70,150] Meanwhile, 2D mesh sensors have a small SNR, large discrete error,^[81] poor accuracy, and low reliability for repeated measurements, which is unfavorable for weak signal monitoring and high-density integration.^[39,149,151]

3.3.2. 3D Mesh

The mesh structure was not limited to a 2D structure. By further introducing a 3D stretchable structure, the stretchable electrode exhibited good conductivity under higher strain. For example, a piece of paper cannot be stretched; however, a paper net is highly stretchable. The greater the number of grids, the greater the degree of stretchability (Figure 11A).^[211] The 3D mesh structure was similar to the porous structure of the pressure sensor.

Commercial organic foam materials are used as dielectrics for both pressure and strain sensing (Figure 11B), and the sensor combines a compressible silicone foam as a dielectric layer with microcracked stretchable gold as the electrode layer, thus achieving a pressure sensitivity from 5 to 405 kPa with a maximum tensile strain of up to 30% (Figure 11C).^[212] Zheng et al. heated and cured a mixture of PDMS and water to form a porous PDMS dielectric layer (Figure 11D). After drying the soaked sensor, its performance could still be restored to the its original state with excellent mechanical circulation (Figure 11E).^[130] Based on the 3D mesh structure, adding other functional materials into the composite materials can provide the sensor with other ideal functions. Park et al. mixed spiropyran, PDMS, and silica nanoparticles (SNPs) in a hydrophilic cosolvent (water and ethanol) to prepare a porous mechanical color-changing composite material with a graded nanoporous–microporous (NP–MP) structure, which could be used to visualize the magnitude of strain (Figure 11F).^[56] Because the local stress in the graded NP–MP structure increases energy dissipation, and modifying the porous composite material with SNPs

can further improve the tensile properties and maximum stress of the material, the hierarchical NP–MP structure in the porous polymer improved the mechanical sensitivity and stretchability (maximum strain 400%) compared with the nonporous structure (240%) (Figure 11G).^[56] Peng et al. designed a sandwich-structured sensor, the core of which was a three-layered porous structure prepared using a simple sugar particle template technology, and two panels contained isolated conductive networks of AgNWs and carbon nanofibers. The new multidirectional sensor had a unique asymmetric sandwich structure that could be employed to simultaneously detect multiple stimulus signals, such as pressure and tension (Figure 11H).^[137] Park et al. used E-skin made of a porous microstructure to distinguish between various forms of tactile information, such as pressure, strain, bend, and sound vibration (Figure 11I).^[94] In addition, the porous surface of PDMS made it nonadhesive to the SWCNT electrode due to its reduced contact area, which was beneficial for repeated measurement and expanded application prospects.

Although the 3D mesh structure can be employed for strain sensing, the maximum deformation achieved in currently research is smaller than that of other structures, usually no more than 50% and only ≈10% for some structures.^[33,37,130] This greatly limits its practical application. In addition, as with the porous structure of the pressure sensor, the uniform size and distribution of the holes remain problems to be solved.

3.4. Textile/Woven Fiber Structure

Since the 17th century, Irish fishermen have woven woolen sweaters. In modern society, weaving is a process in which coils are formed by yarn using knitting needles, which are then connected to textiles through stringing. Compared with other clothing, textiles have a 3D mesh structure. This porous structure endows textiles with ductility, mechanical toughness, breathability, softness, and comfort.^[152] The appropriate combinations of textiles and clothes can be used for real-time monitoring of human pulse, movement, and other daily activities; these textiles have great potential for application in wearable devices.^[31,151] Lee's group demonstrated the feasibility of texture-based sensors in wearable devices by integrating them into gloves and clothes in the form of fabrics to control the machine wirelessly (Figure 12A), which proved the feasibility of textile-based sensors in wearable devices.^[14]

Capacitive sensing systems based on textiles can be established not only at the textile level^[152] but also at the fiber level,^[14,213] which is conducive to the construction of orthogonal textile arrays^[214] and facilitates integration with clothes. Special response characteristics and directional sensitivity can be achieved by fabricating a sensor with a woven structure by embedding conductive materials with porous structures into the elastomer matrix.^[13,215–219] Cooper et al. melted liquid metal into hollow elastic capillaries to obtain fibers integrated with fabrics and then wound it into spirals to create a capacitive sensor with the capability of sensing torsion, strain, and tactility (Figure 12B). When twisted or stretched, the geometry of fibers and the capacitance between the fibers change accordingly, thereby achieving good sensing performance (Figure 12C).^[213]

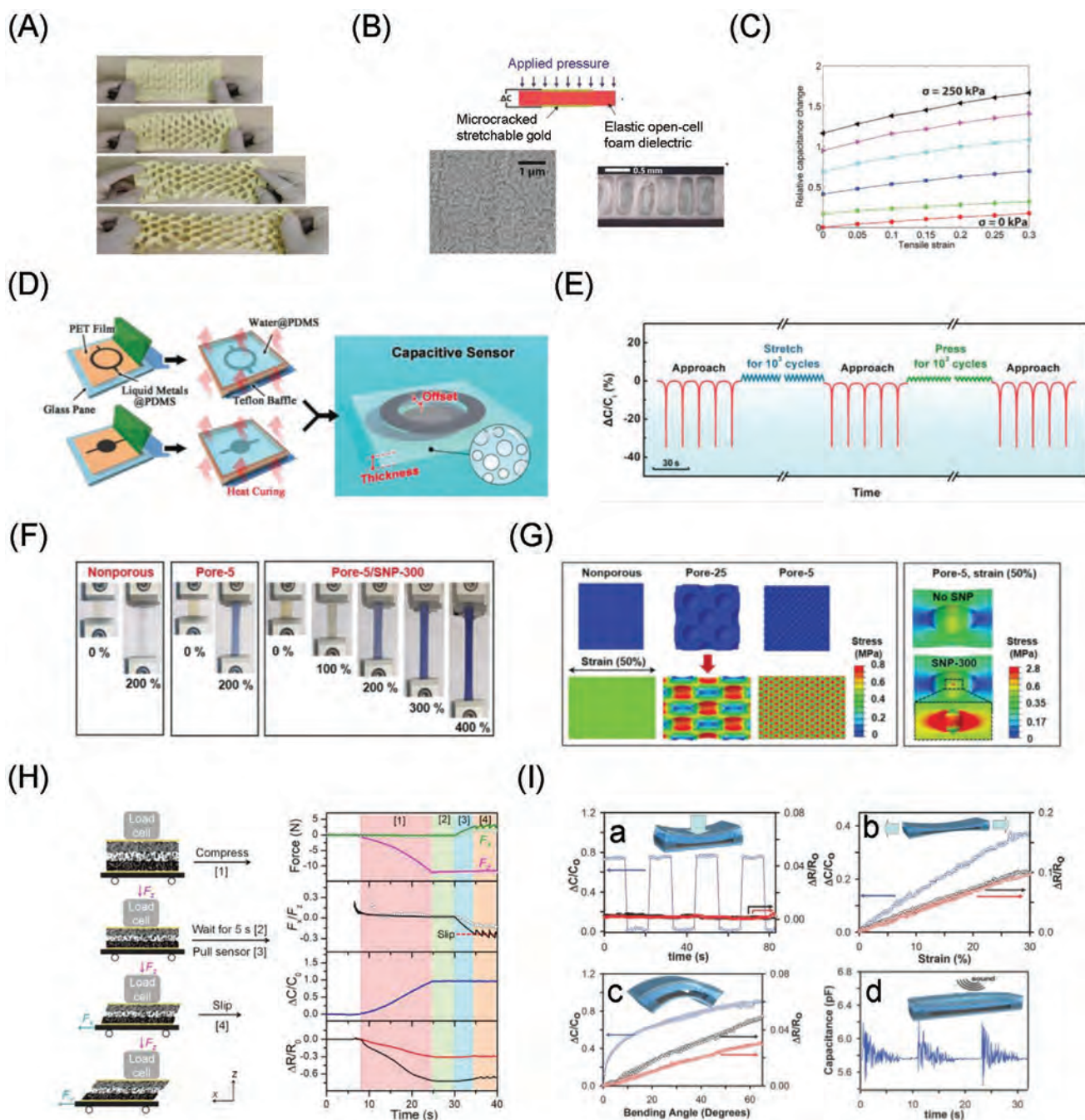


Figure 11. A) Stretching two sheets of letter-sized papers containing an array of slits with coarse and fine ligaments, respectively. B) Schematic of the stretchable capacitive pressure sensors. C) Relative capacitance change as a function of applied tensile strain at different compressive states. A–C) Adapted with permission.^[12] Copyright 2015, Wiley-VCH. D) Schematic illustration of the fabrication procedure for preparing the wearable capacitive sensor. E) Relative capacitance change rate during approach-leave operations, repeated stretching cycle operations, and repeated pressure cycle operations. D,E) Reproduced under the terms of the CC-BY Creative Commons Attribution 4.0 International license (<https://creativecommons.org/licenses/by/4.0/>).^[30] Copyright 2020, The Authors, published by Wiley-VCH. F) Photographs of mechanochromic polymers with different structures exhibiting color changes in response to tensile strain. G) FEA-determined stress distributions of mechanochromic polymers with different pore sizes (left) and with 300 nm SNPs and a 5 μ m pore size (right). F,G) Reproduced with permission.^[56] Copyright 2019, Wiley-VCH. H) Experimental setup for detection of compression, shear, and slippage, and corresponding measurements of force, relative capacitance, and resistance. Adapted with permission.^[37] Copyright 2020, American Chemical Society. I) Detection of various mechanical stimuli under: a) repeated normal pressure, b) strain, c) bending, and d) sound vibration. Adapted with permission.^[94] Copyright 2014, Wiley-VCH.

For textile-based strain sensors, the applied strain will cause macroscopic deformation of the network structure rather

than individual fibers, thereby suppressing the local stress during the stretching process and improving its stretchability

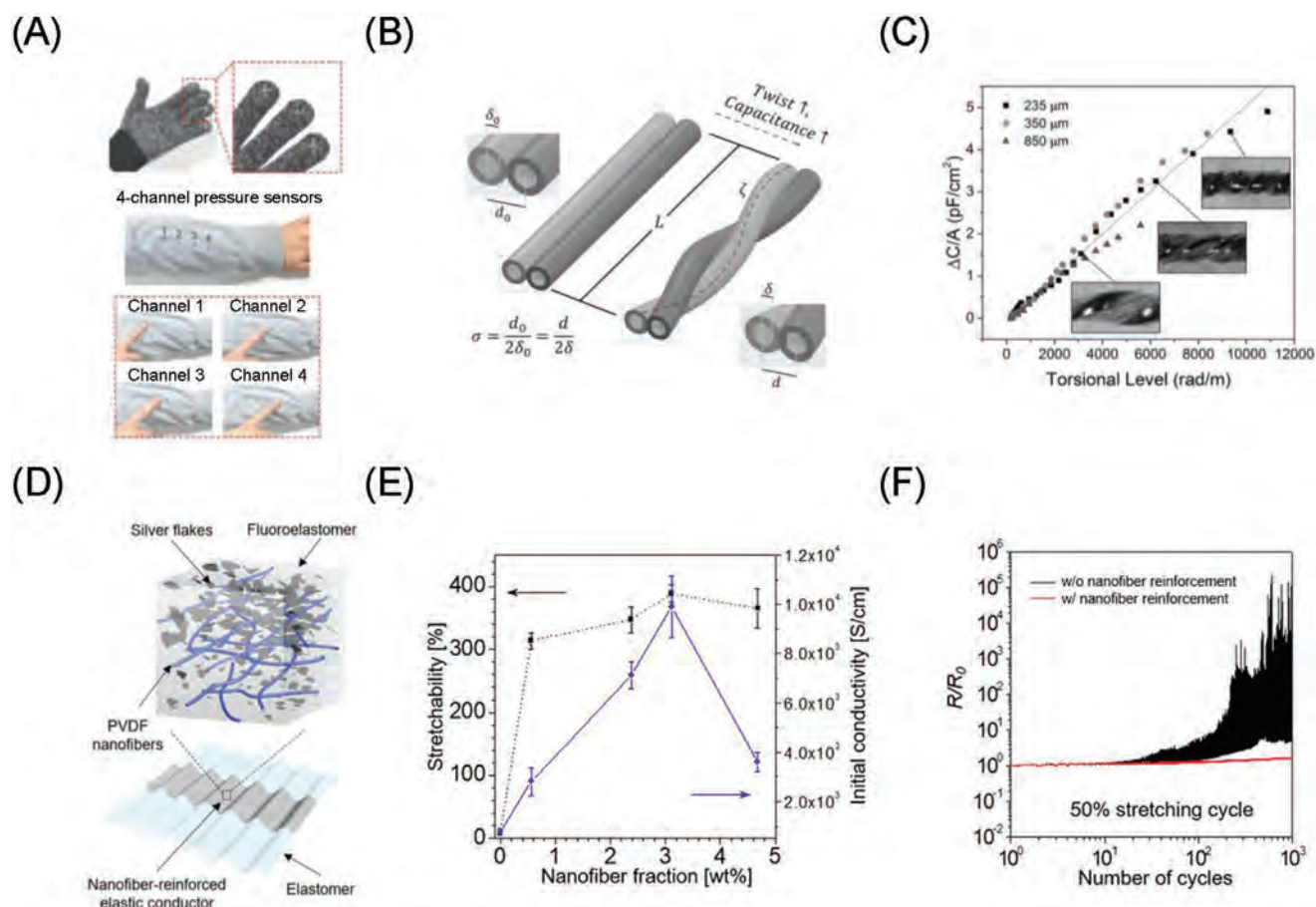


Figure 12. A) Photograph showing the smart glove with the textile-based pressure sensors on the ends of four fingers (the index, middle, ring, and little finger) and clothes with 4-channel pressure sensors. Adapted with permission.^[14] Copyright 2015, Wiley-VCH. B) Schematic of the torsion sensing mechanism with two twisted fibers. Changes in geometry by twisting increase the capacitance between the intertwined fibers. C) Capacitance change per length normalized by the diameter of the fibers collapses the data onto a regression line. B,C) Adapted with permission.^[213] Copyright 2017, Wiley-VCH. D) Schematic of the tough elastic conductor. E) Stretchability and conductivity dependences on the nanofiber fraction for the free-standing film. F) Cyclic stabilities of the buckled structures of the tough elastic conductors with and without nanofiber reinforcement. D–F) Adapted with permission.^[221] Copyright 2019, American Chemical Society.

and stability.^[169,220] Polyvinylidene fluoride (PVDF) has a high dielectric constant among polymers, however, it cannot withstand large tensile strain. For use in capacitive strain sensors, Someya's group layered a PVDF nanofiber-reinforced elastic conductor film and a stretchable dielectric layer on top of a prestretched elastomer and obtained a capacitor with a wrinkle electrode after release (Figure 12D).^[221] The PVDF nanofiber sheet can eliminate stress and suppress crack propagation, which ensures that the sensor maintains good electrical conductivity under high strain (Figure 12E) with great stability (Figure 12F).^[221] This biaxial prestrain can also be used to demonstrate biaxial stretchability and can even be applied to harsh mechanical deformations.

Although the good mechanical properties of composite fabrics and silicone elastomers reduce the application limitations of traditional sensors on wearable devices, the fibers in the textile industry are usually thick and have a size range of tens to hundreds of micrometers, which leads to a large elastic modulus. The sensors may undergo plastic deformation or permanent irreversible deformation when stretched to a certain

strain.^[70] This leads to considerable challenges in the process of manufacturing complex structures in the fibers by the conventional fiber spinning process, and the weaving process limits the freedom degree of the design because the fiber/yarn path is constrained along the warp or weft direction within the fabric.^[222] In addition, the incompatibility between the sensors and soft textile fibers may cause delamination and mechanical failure.^[223] The low durability and low wear resistance of sensors with textiles under repeated stretching are also serious problems^[152] because clothing is affected by chemical corrosion, thermal fatigue, and other factors, resulting in local damage or microcracks, which affect the service life of electronic textiles.

3.5. Discussion

The performances of strain sensors based on microstructures are shown in Table 5. A comparison of the effects of the four common microstructures on the capacitive strain sensors is presented in Table 6. The above-mentioned “stretched structure”

Table 5. Summary of the performance of the strain sensors based on microstructures.

Type	Polymer matrix	Materials	Cyclic stability	Detection limit	Max strain [%]	Remark	Year	Refs.
3D mesh	Serpentine	Ecoflex	Liquid-phase gallium–indium–tin alloy	4	–	200	Capacitance and inductance	2013 [68]
		PI	Si	5	–	80	Humidity sensor	2014 [203]
		PDMS	Ag	1000	6 Pa	70%; 100 kPa ^{b)}	–	2015 [204]
		PI		54 000 (300% strain) ^{a)} ; 450 (150 μ m bend) ^{a)}	–	800%; 400 kPa ^{b)}	Simultaneous multi-stimulus sensing; adjustable sensing range; large-area expandability	2018 [209]
	2D mesh		Au				No wrinkle or fold after deformation;	
		PDMS		1000 (100% strain) ^{a)}	–	100	High transparency	2019 [166]
	PI + Ecoflex			–	–	25	–	2012 [69]
	–	PDMS	SWCNT	–	2.5 Pa	30	Differentiating multiple Mechanical stimuli	2014 [94]
	Water-in-oil emulsion method		Carbon black	100	–	10	–	2018 [33]
	Deionized water + ethanol		Spiropyran + SNPs	–	–	With porous-400; without porous-240	Mechanochromic	2019 [56]
Woven fibers	Water		Liquid metals	1000	–	10	Noncontact detectivity	2020 [130]
	Sugar		AgNWs/CNTs	–	–	50	Measurement of multiple forces	2020 [137]
	Purchased	Silicone	Au + EGaIn	–	–	30	Decoupling the strain and pressure cross-sensitivity	2015 [212]
	DMF	PVDF	Ionic liquid	–	–	18	Transparency	2020 [37]
	Woven	PDMS	PEDOT:PSS	–	–	20	–	2016 [13]
		Commercial textiles	PVDF-HFP + [EMIM][TFSI]	–	2.4 Pa	–	–	2017 [151]
				1000	–	100	–	2017 [70]
	Nylon	Ecoflex	Ag	–	–	30	–	2017 [31]
	Nanofibers	PVDF	Ag + fluoroelastomer	5000 (50% strain) ^{a)}	–	800	–	2019 [221]





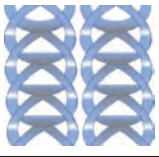
^{a)}The contents in parentheses indicate the test conditions for cyclic stability experiments; ^{b)}The sensor can be used for both strain sensing and pressure sensing.

has good biocompatibility, which makes up for the limitations of traditional rigid elements in motion and mechanical adaptation to the human skin.^[3,224] However, the manufacturing processes of stretched structures are usually complicated and low-yield, which increases costs, and have a negative influence on mass production.^[225] Moreover, some stretched structures are limited in the stretching direction and have unstable electrical functionality and mechanical integrity under large periodic mechanical deformation.^[226] The main reasons for the degradation in performance of strain sensors are the fatigue and plastic deformation of polymer substrates, as well as the fracture and buckling of sensing nanomaterials under high strain, which makes the strain sensors unsuitable for long-term applications. Some studies have combined 3D geometric engineering with elastomer substrates to achieve electrically stable and high-performance stretchable electrodes.^[227,228] Considering the diversity

and mismatch of the Young's modulus of different components, unfixed connections between fibers will slip or separate under the mechanical strain applied by static and loading/unloading cycles for a long time. Thus, the SNR is limited, which causes a significant interference to the actual strain signal^[169] and affects the accuracy of the output data.

Compared with pressure sensors, the development of strain sensors remains sluggish. The main goal of the stretched structure method is to endow the sensors of nonstretchable materials with stretchability, which is different from the characterization of pressure sensors. The goals of research on pressure sensors are to improve the sensitivity, shorten the response time, and improve the linearity of the output curve. However, the current characterization of strain sensors focuses on stretchability and repeatability, the minimum detection amount of strain sensing is not focused upon.

Table 6. Comparison of the four common microstructure influences on strain capacitive sensors.

Type	Schematic	Advantages	Disadvantages	Summary	Challenge
Wrinkle		First proposed Prepared simply	Uncontrollable microstructure Stretchable in one direction	Uneven Uncontrolled Low-cost Simple	Methods of obtaining stretchability deteriorate sensitivity
Serpentine		Enhanced ductility Directed response	Susceptible to interference	Uniform Controllable Expensive Complex	
Mesh	2D  3D 	Stretchable in all directions Large deformation		Uneven Uncontrolled Low-cost Simple	
Woven fibers		Combined with clothing	Irreversible deformation		

4. Challenges and Outlook

New fabrication techniques and new information transmission methods (e.g., wireless technology) have promoted the development of capacitive sensors. However, some problems remain to be resolved. Common microstructured capacitive sensors have the following conflicts (**Figure 13**):

- 1) Conflict between high sensitivity and stretchability: For pressure sensors, different microstructures are used to achieve high sensitivity and low hysteresis;^[36,40,55,106] however, they cannot be used in large strain situations. Strain sensors use microstructures to convert materials with poor stretchability into structures that can withstand large strains^[153,185,195,196] but with low sensitivity. No published works have combined the advantages of high sensitivity and stretchability because high sensitivity requires the sensor to cause large changes in capacitance by producing significant large structural changes under small strain.^[91] Stretchability is required to maintain the integrity of the structure and the morphology of the material under large strains. Realizing high sensitivity and stretchability simultaneously by designing an outstanding microstructure in the same capacitive sensor in the future is still a challenging task.
- 2) Conflict between hysteresis and anti-interference: A higher amount of air phase in the microstructure means a smaller

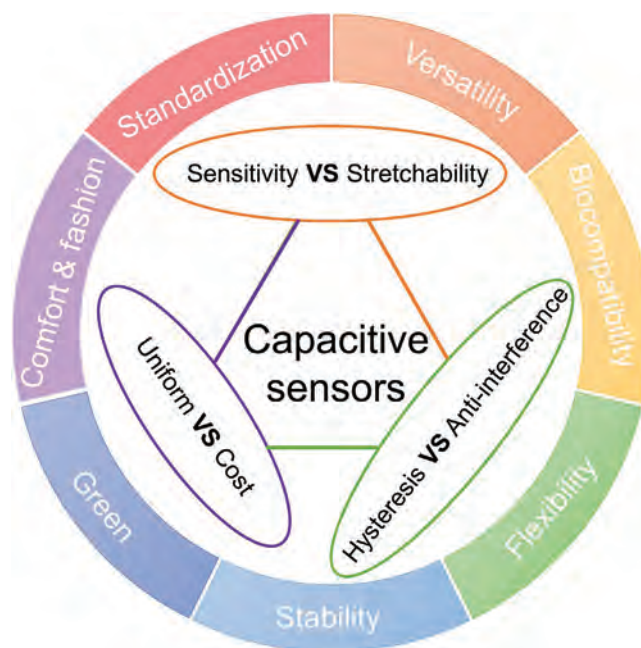


Figure 13. Current conflicts and future prospects of capacitive sensors.

amount of polymer in the same volume. The air can reduce the contact area between the microstructure layer and the opposite layer, thereby reducing the viscoelasticity and hysteresis of the sensors.^[106] However, microstructured design has inherent drawbacks such as the permittivity of air being much smaller than that of the polymer matrix, which reduces the initial capacitance of the sensor, leading to poor anti-interference ability and low SNR. This problem affects the measurement accuracy, which limits its application in weak signal detection and high-density integration.^[39,149,151]

- 3) Conflict between uniformity and cost: Although the commonly used methods to prepare microstructures have prominent advantages in obtaining fine structures, the preparation processes usually require multiple steps, such as sophisticated and time-consuming photolithography and chemical etching,^[38,107,134–136] which greatly increases the cost and duration of production. In contrast, preparation methods for porous and natural plant-based structures are usually simple and inexpensive.^[47,52,71,130,132,137] However, these methods are usually poorly controlled. The uneven distribution of pores and the randomness of natural microstructures fail to generate the desired morphologies in the prepared microstructures,^[39] which lead to poor stability and low reliability in different batches of products.^[82,114] Therefore, such conflicts greatly limit the mass production and performance of the sensors.

These challenges also provide opportunities for the future development of capacitive sensors (Figure 13):

- 1) Standardization: Currently, the characterization parameters of capacitive sensors mainly include sensitivity, linearity, detection limit, hysteresis, and stability, whereas the criteria for evaluating performance are different. Hence, a specific standard is required to determine the capacitive sensors in the corresponding application fields. For example, if capacitive sensors are employed in wearable devices, the device should be able to withstand at least 50% strain and tens of thousands of cycles of stability to meet the deformation range and cycles of human skin.
- 2) Versatility: Numerous research efforts have been devoted to multifunctional signal pressure, strain, and touch sensors for temperature, humidity, airflow, acoustic waves, and other sensing fields. E-skins are increasingly able to imitate or even surpass the functions of human skin, improving sensing performance and expanding application areas.
- 3) Biocompatibility: Flexible devices fit well with human skin. For example, retractable temperature sensors have great application prospects compared to traditional rigid thermal sensors.^[167] Moreover, biodegradable sensors implanted into the body can be degraded through human metabolism during the postoperative recovery phase, which causes no secondary harm to the patients.
- 4) Flexibility: Most capacitive sensors currently studied require an additional power supply. Bulky batteries and complex wiring limit system flexibility. However, wireless technology and self-powered technology can solve these problems, without affecting the normal activities of the human body.

- 5) Environmental protection: The development of microstructures is usually a low-yield and high-cost process, which involves complex multistep fabrication steps such as lithography, transfer, and vacuum deposition,^[153] which greatly limit their practical application. Using low-cost, low-loss materials or reusable electronic components with fewer manufacturing steps can greatly reduce electronic waste and make the process cost-effective.
- 6) Cyclic stability and chemical stability: The test of cycle durability usually involves load/release cycles with pressure or tension on sensors using testing machines in the laboratory. However, the magnitude and direction of stress and strain are uncertain in real life. Pollutants in the natural environment (e.g., dust, gas, and microorganisms) and pollutants on the human skin surface (e.g., grease, sweat, and body fluids) are complex.^[151,169] Encapsulation technology is required to isolate the sensor from the external environment and solve these problems without affecting communication and data processing.
- 7) Comfort and fashion: The appearance of a product is also an important evaluation indicator of daily use.^[152] In addition to intelligence, the sensor should also be softness and comfort, should be designed with a good sense of fashion, have an elegant appearance, and cause less hindrance to daily life activities.

5. Conclusions

We have summarized the advantages, disadvantages, and practical applications of several popular microstructures that are widely employed in capacitive sensors. The microstructured dielectric layer or electrode can improve sensor sensitivity, reduce hysteresis, and endow the rigid electronic device with excellent elastic stretchability, which is an essential part of the next-generation wearable devices and soft robots. Because the volume of polymers is almost unchanged when pressure is applied, the polymer dielectrics are inherently viscoelastic. These shortcomings severely limit the improvement in sensitivity and high hysteresis. Therefore, more efforts have been applied to strengthen the sensing performance by designing different microstructures of materials. To accelerate the development of flexible and stretchable capacitive sensors with different microstructures, as we pointed out in this review, three types of conflicts between high sensitivity and stretchability, between hysteresis and anti-interference, and between uniform and cost should be focused upon. In addition, the various challenges presented in this review also provide opportunities for the future development of capacitive sensors. Finally, the rise of new technologies such as wireless communication and supercapacitors has promoted the rapid development of capacitive sensors, indicating that multifunctional E-skins with similar or even better performance than human skin with broader application prospects can be developed. We expect that this review will provide a comprehensive understanding for designing advanced flexible and stretchable capacitive sensors using ingenious human-made microstructures.

Acknowledgements

This work was supported by the National Natural Science Foundation of China (Grant Nos. 51921005 and 51802023), the Fund of IPOC BUPT (Grant No. IPOC2020ZT09), and the Fundamental Research Funds for the Central Universities under Grant No. 2019RC23.

Conflict of Interest

The authors declare no conflict of interest.

Keywords

capacitive sensors, geometric design, microstructures, sensitivity, stretchable materials

Received: December 7, 2020

Revised: March 5, 2021

Published online:

- [1] J. Heikenfeld, A. Jajack, J. Rogers, P. Gutruf, L. Tian, T. Pan, R. Li, M. Khine, J. Kim, J. Wang, J. Kim, *Lab Chip* **2018**, *18*, 217.
- [2] A. Chortos, J. Liu, Z. Bao, *Nat. Mater.* **2016**, *15*, 937.
- [3] S. Chen, L. Sun, X. Zhou, Y. Guo, J. Song, S. Qian, Z. Liu, Q. Guan, E. Meade Jeffries, W. Liu, Y. Wang, C. He, Z. You, *Nat. Commun.* **2020**, *11*, 1107.
- [4] Y. Liu, M. Pharr, G. A. Salvatore, *ACS Nano* **2017**, *11*, 9614.
- [5] S. Yao, L. Vargas, X. Hu, Y. Zhu, *IEEE Sens. J.* **2018**, *18*, 3010.
- [6] R. Dahiya, N. Yogeswaran, F. Liu, L. Manjakkal, E. Burdet, V. Hayward, H. Jorntell, *Proc. IEEE* **2019**, *107*, 2016.
- [7] A. Gallace, C. Spence, *In Touch with the Future: The Sense of Touch from Cognitive Neuroscience to Virtual Reality*, Oxford University Press, Oxford, UK **2014**.
- [8] Y. Wan, Y. Wang, C. F. Guo, *Mater. Today Phys.* **2017**, *1*, 61.
- [9] J. Y. Oh, Z. Bao, *Adv. Sci.* **2019**, *6*, 1900186.
- [10] X. Wang, L. Dong, H. Zhang, R. Yu, C. Pan, Z. L. Wang, *Adv. Sci.* **2015**, *2*, 1500169.
- [11] X. Zeng, Z. Wang, H. Zhang, W. Yang, L. Xiang, Z. Zhao, L. M. Peng, Y. Hu, *ACS Appl. Mater. Interfaces* **2019**, *11*, 21218.
- [12] M. S. Cao, X. X. Wang, M. Zhang, W. Q. Cao, X. Y. Fang, J. Yuan, *Adv. Mater.* **2020**, *32*, 1907156.
- [13] S. Takamatsu, T. Lonjaret, E. Ismailova, A. Masuda, T. Itoh, G. G. Malliaras, *Adv. Mater.* **2016**, *28*, 4485.
- [14] J. Lee, H. Kwon, J. Seo, S. Shin, J. H. Koo, C. Pang, S. Son, J. H. Kim, Y. H. Jang, D. E. Kim, T. Lee, *Adv. Mater.* **2015**, *27*, 2433.
- [15] R. Dahiya, *Proc. IEEE* **2019**, *107*, 247.
- [16] L. Beccai, C. Lucarotti, M. Tataro, M. Taghavi, in *Soft Robotics: Trends, Applications and Challenges* (Eds: C. Laschi, J. Rossiter, F. Iida, M. Cianchetti, L. Margheri), Springer, Cham, Switzerland **2017**.
- [17] Z. Lei, P. Wu, *Mater. Horiz.* **2019**, *6*, 538.
- [18] Y. Ma, Y. Zhang, S. Cai, Z. Han, X. Liu, F. Wang, Y. Cao, Z. Wang, H. Li, Y. Chen, X. Feng, *Adv. Mater.* **2020**, *32*, 1902062.
- [19] M. L. Hammock, A. Chortos, B. C. K. Tee, J. B. H. Tok, Z. Bao, *Adv. Mater.* **2013**, *25*, 5997.
- [20] M. G. Broadhurst, G. T. Davis, *Ferroelectrics* **1984**, *60*, 3.
- [21] M. Wegener, W. Wirges, R. Gerhard-Mulhaupt, *Adv. Eng. Mater.* **2005**, *7*, 1128.
- [22] X. Zhang, J. Hillenbrand, G. M. Sessler, *J. Appl. Phys.* **2007**, *101*, 054114.
- [23] D. Wang, Z. Fan, G. Rao, G. Wang, Y. Liu, C. Yuan, T. Ma, D. Li, X. Tan, Z. Lu, A. Feteira, S. Liu, C. Zhou, S. Zhang, *Nano Energy* **2020**, *76*, 104944.
- [24] Y. Ma, W. Tong, W. Wang, Q. An, Y. Zhang, *Compos. Sci. Technol.* **2018**, *168*, 397.
- [25] S. Xu, Y. Qin, C. Xu, Y. Wei, R. Yang, Z. L. Wang, *Nat. Nanotechnol.* **2010**, *5*, 366.
- [26] G. R. Witt, *Thin Solid Films* **1974**, *22*, 133.
- [27] W. Obitayo, T. Liu, *J. Sens.* **2012**, *2012*, 652438.
- [28] L. Duan, D. R. D'hooge, L. Cardon, *Prog. Mater. Sci.* **2020**, *114*, 100617.
- [29] J. G. Dabbling, A. Filatov, J. W. Wheeler, in *2012 Annu. Int. Conf. of the IEEE Engineering in Medicine and Biology Society*, IEEE, Piscataway, NJ, USA **2012**, pp. 162–165.
- [30] M. Cao, X. Wang, W. Cao, X. Fang, B. Wen, J. Yuan, *Small* **2018**, *14*, 1800987.
- [31] M. Tataro, T. Poliero, A. Mondini, C. Lucarotti, G. Cairoli, J. Ortiz, L. Beccai, *Sensors* **2017**, *17*, 2314.
- [32] C. S. Sander, J. W. Knutti, J. D. Meindl, *IEEE Trans. Electron Devices* **1980**, *27*, 927.
- [33] M. Pruvost, W. J. Smit, C. Monteux, P. Poulin, A. Colin, *npj Flexible Electron.* **2019**, *3*, 13.
- [34] R. Puers, *Sens. Actuators, A* **1993**, *37–38*, 93.
- [35] J. Y. Sun, C. Keplinger, G. M. Whitesides, Z. Suo, *Adv. Mater.* **2014**, *26*, 7608.
- [36] S. C. B. Mannsfeld, B. C. K. Tee, R. M. Stoltenberg, C. V. H. H. Chen, S. Barman, B. V. O. Muir, A. N. Sokolov, C. Reese, Z. Bao, *Nat. Mater.* **2010**, *9*, 859.
- [37] Q. Liu, Z. Liu, C. Li, K. Xie, P. Zhu, B. Shao, J. Zhang, J. Yang, J. Zhang, Q. Wang, C. F. Guo, *Adv. Sci.* **2020**, *7*, 2000348.
- [38] C. Pang, J. H. Koo, A. Nguyen, J. M. Caves, M. G. Kim, A. Chortos, K. Kim, P. J. Wang, J. B. H. Tok, Z. Bao, *Adv. Mater.* **2015**, *27*, 634.
- [39] Y. Guo, S. Gao, W. Yue, C. Zhang, Y. Li, *ACS Appl. Mater. Interfaces* **2019**, *11*, 48594.
- [40] G. Liang, Y. Wang, D. Mei, K. Xi, Z. Chen, *J. Microelectromech. Syst.* **2015**, *24*, 1510.
- [41] B. Zhuo, S. Chen, M. Zhao, X. Guo, *IEEE J. Electron Devices Soc.* **2017**, *5*, 219.
- [42] H. K. Lee, S. Il Chang, E. Yoon, *J. Microelectromech. Syst.* **2006**, *15*, 1681.
- [43] H. K. Lee, S. Il Chang, E. Yoon, *IEEE Sens. J.* **2009**, *9*, 1748.
- [44] J. A. Dobrzynska, M. A. M. Gijss, *Sens. Actuators, A* **2012**, *173*, 127.
- [45] R. Li, B. Nie, C. Zhai, J. Cao, J. Pan, Y. W. Chi, T. Pan, *Ann. Biomed. Eng.* **2016**, *44*, 2282.
- [46] H. H. Chou, A. Nguyen, A. Chortos, J. W. F. To, C. Lu, J. Mei, T. Kurosawa, W. G. Bae, J. B. H. Tok, Z. Bao, *Nat. Commun.* **2015**, *6*, 8011.
- [47] B. Y. Lee, J. Kim, H. Kim, C. Kim, S. D. Lee, *Sens. Actuators, A* **2016**, *240*, 103.
- [48] C. C. Kim, H. H. Lee, K. H. Oh, J. Y. Sun, *Science* **2016**, *353*, 682.
- [49] A. D. Mazzeo, W. B. Kalb, L. Chan, M. G. Killian, J. F. Bloch, B. A. Mazzeo, G. M. Whitesides, *Adv. Mater.* **2012**, *24*, 2850.
- [50] R. Shi, Z. Lou, S. Chen, G. Shen, *Sci. China Mater.* **2018**, *61*, 1587.
- [51] M. Li, J. Liang, X. Wang, M. Zhang, *Sensors* **2020**, *20*, 371.
- [52] J. Il Yoon, K. S. Choi, S. P. Chang, *Microelectron. Eng.* **2017**, *179*, 60.
- [53] L. Xie, P. Chen, S. Chen, K. Yu, H. Sun, *Sensors* **2019**, *19*, 3427.
- [54] X. H. Hu, X. Zhang, M. Liu, Y. F. Chen, P. Li, W. H. Pei, C. Zhang, H. D. Chen, *Sci. China Inf. Sci.* **2014**, *57*, 120204.
- [55] Y. Wan, Z. Qiu, Y. Hong, Y. Wang, J. Zhang, Q. Liu, Z. Wu, C. F. Guo, *Adv. Electron. Mater.* **2018**, *4*, 1700586.
- [56] J. Park, Y. Lee, M. H. Barbee, S. Cho, S. Cho, R. Shanker, J. Kim, J. Myoung, M. P. Kim, C. Baig, S. L. Craig, H. Ko, *Adv. Mater.* **2019**, *31*, 1808148.
- [57] Y. Xiong, Y. Shen, L. Tian, Y. Hu, P. Zhu, R. Sun, C. P. Wong, *Nano Energy* **2020**, *70*, 104436.

- [58] W. Yang, N. W. Li, S. Zhao, Z. Yuan, J. Wang, X. Du, B. Wang, R. Cao, X. Li, W. Xu, Z. L. Wang, C. Li, *Adv. Mater. Technol.* **2018**, 3, 1700241.
- [59] C. G. Núñez, W. T. Navaraj, E. O. Polat, R. Dahiya, *Adv. Funct. Mater.* **2017**, 27, 1606287.
- [60] H. Jang, H. Yoon, Y. Ko, J. Choi, S. S. Lee, I. Jeon, J. H. Kim, H. Kim, *Nanoscale* **2016**, 8, 5667.
- [61] L. Viry, A. Levi, M. Totaro, A. Mondini, V. Mattoli, B. Mazzolai, L. Beccai, *Adv. Mater.* **2014**, 26, 2659.
- [62] H. Z. Zhang, Q. Y. Tang, Y. C. Chan, *AIP Adv.* **2012**, 2, 022112.
- [63] D. Son, J. Kang, O. Vardoulis, Y. Kim, N. Matsuhisa, J. Y. Oh, J. W. To, J. Mun, T. Katsumata, Y. Liu, A. F. McGuire, M. Krasen, F. Molina-Lopez, J. Ham, U. Kraft, Y. Lee, Y. Yun, J. B. H. Tok, Z. Bao, *Nat. Nanotechnol.* **2018**, 13, 1057.
- [64] C. Larson, B. Peele, S. Li, S. Robinson, M. Totaro, L. Beccai, B. Mazzolai, R. Shepherd, *Science* **2016**, 351, 1071.
- [65] D. Kwon, T. I. Lee, J. Shim, S. Ryu, M. S. Kim, S. Kim, T. S. Kim, I. Park, *ACS Appl. Mater. Interfaces* **2016**, 8, 16922.
- [66] M. Ntagios, H. Nassar, A. Pullanchiyodan, W. T. Navaraj, R. Dahiya, *Adv. Intell. Syst.* **2020**, 2, 1900080.
- [67] S. R. A. Ruth, L. Beker, H. Tran, V. R. Feig, N. Matsuhisa, Z. Bao, *Adv. Funct. Mater.* **2019**, 30, 1903100.
- [68] A. Fassler, C. Majidi, *Smart Mater. Struct.* **2013**, 22, 055023.
- [69] M. Ying, A. P. Bonifas, N. Lu, Y. Su, R. Li, H. Cheng, A. Ameen, Y. Huang, J. A. Rogers, *Nanotechnology* **2012**, 23, 344004.
- [70] A. Atalay, V. Sanchez, O. Atalay, D. M. Vogt, F. Haufe, R. J. Wood, C. J. Walsh, *Adv. Mater. Technol.* **2017**, 2, 1700136.
- [71] J. Choi, D. Kwon, K. Kim, J. Park, D. Del Orbe, J. Gu, J. Ahn, I. Cho, Y. Jeong, Y. Oh, I. Park, *ACS Appl. Mater. Interfaces* **2020**, 12, 1698.
- [72] Z. Yuan, G. Shen, C. Pan, Z. L. Wang, *Nano Energy* **2020**, 73, 104764.
- [73] T. Y. Choi, B. U. Hwang, B. Y. Kim, T. Q. Trung, Y. H. Nam, D. N. Kim, K. Eom, N. E. Lee, *ACS Appl. Mater. Interfaces* **2017**, 9, 18022.
- [74] C. M. Boutry, M. Negre, M. Jorda, O. Vardoulis, A. Chortos, O. Khatib, Z. Bao, *Sci. Rob.* **2018**, 3, eaau6914.
- [75] H. Vandepparre, D. Watson, S. P. Lacour, *Appl. Phys. Lett.* **2013**, 103, 204103.
- [76] X. Zhang, S. Hu, M. Wang, J. Yu, Q. Khan, J. Shang, L. Ba, *Nanotechnology* **2015**, 26, 115501.
- [77] L. Wang, *IEEE Electron Device Lett.* **2017**, 38, 123.
- [78] F. B. Madsen, A. E. Daugaard, S. Hvilsted, A. L. Skov, *Macromol. Rapid Commun.* **2016**, 37, 378.
- [79] M. I. Tiwana, S. J. Redmond, N. H. Lovell, *Sens. Actuators, A* **2012**, 179, 17.
- [80] N. Q. Balaban, U. S. Schwarz, D. Riveline, P. Goichberg, G. Tzur, I. Sabanay, D. Mahalu, S. Safran, A. Bershadsky, L. Addadi, B. Geiger, *Nat. Cell Biol.* **2001**, 3, 466.
- [81] A. Rana, J. P. Roberge, V. Duchaine, *IEEE Sens. J.* **2016**, 16, 7853.
- [82] X. Shuai, P. Zhu, W. Zeng, Y. Hu, X. Liang, Y. Zhang, R. Sun, C. P. Wong, *ACS Appl. Mater. Interfaces* **2017**, 9, 26314.
- [83] J. He, Y. Zhang, R. Zhou, L. Meng, T. Chen, W. Mai, C. Pan, *J. Mater.* **2020**, 6, 86.
- [84] T. Li, H. Luo, L. Qin, X. Wang, Z. Xiong, H. Ding, Y. Gu, Z. Liu, T. Zhang, *Small* **2016**, 12, 5042.
- [85] I. Clausen, T. Glott, *Sensors* **2014**, 14, 17686.
- [86] D. P. J. Cotton, I. M. Graz, S. P. Lacour, *IEEE Sens. J.* **2009**, 9, 2008.
- [87] H. Jin, S. Jung, J. Kim, S. Heo, J. Lim, W. Park, H. Y. Chu, F. Bien, K. Park, *Sci. Rep.* **2017**, 7, 10854.
- [88] D. J. Cohen, D. Mitra, K. Peterson, M. M. Maharbiz, *Nano Lett.* **2012**, 12, 1821.
- [89] J. Yuan, A. Luna, W. Neri, C. Zakri, A. Colin, P. Poulin, *ACS Nano* **2018**, 12, 1688.
- [90] H. Charaya, T. G. La, J. Rieger, H. J. Chung, *Adv. Mater. Technol.* **2019**, 4, 1900327.
- [91] L. Beker, N. Matsuhisa, I. You, S. R. A. Ruth, S. Niu, A. Foudeh, J. B. H. Tok, X. Chen, Z. Bao, *Proc. Natl. Acad. Sci. USA* **2020**, 117, 11314.
- [92] W. Deng, X. Huang, W. Chu, Y. Chen, L. Mao, Q. Tang, W. Yang, *J. Sens.* **2016**, 2016, 2428305.
- [93] G. Y. Bae, J. T. Han, G. Lee, S. Lee, S. W. Kim, S. Park, J. Kwon, S. Jung, K. Cho, *Adv. Mater.* **2018**, 30, 1803388.
- [94] S. Park, H. Kim, M. Vosgueritchian, S. Cheon, H. Kim, J. H. Koo, T. R. Kim, S. Lee, G. Schwartz, H. Chang, Z. Bao, *Adv. Mater.* **2014**, 26, 7324.
- [95] S. Zhao, W. Ran, D. Wang, R. Yin, Y. Yan, K. Jiang, Z. Lou, G. Shen, *ACS Appl. Mater. Interfaces* **2020**, 12, 32023.
- [96] Y. Gao, G. Yu, T. Shu, Y. Chen, W. Yang, Y. Liu, J. Long, W. Xiong, F. Xuan, *Adv. Mater. Technol.* **2019**, 4, 1900504.
- [97] B. Nie, R. Li, J. Cao, J. D. Brandt, T. Pan, *Adv. Mater.* **2015**, 27, 6055.
- [98] S. R. A. Ruth, V. R. Feig, H. Tran, Z. Bao, *Adv. Funct. Mater.* **2020**, 30, 2003491.
- [99] C. L. Choong, M. B. Shim, B. S. Lee, S. Jeon, D. S. Ko, T. H. Kang, J. Bae, S. H. Lee, K. E. Byun, J. Im, Y. J. Jeong, C. E. Park, J. J. Park, U. I. Chung, *Adv. Mater.* **2014**, 26, 3451.
- [100] H. Kim, G. Kim, T. Kim, S. Lee, D. Kang, M. S. Hwang, Y. Chae, S. Kang, H. Lee, H. G. Park, W. Shim, *Small* **2018**, 14, 1703432.
- [101] B. C. K. Tee, A. Chortos, R. R. Dunn, G. Schwartz, E. Eason, Z. Bao, *Adv. Funct. Mater.* **2014**, 24, 5427.
- [102] Y. Zhang, Y. Hu, P. Zhu, F. Han, Y. Zhu, R. Sun, C. P. Wong, *ACS Appl. Mater. Interfaces* **2017**, 9, 35968.
- [103] S. Peng, P. Blanloeuil, S. Wu, C. H. Wang, *Adv. Mater. Interfaces* **2018**, 5, 1870088.
- [104] G. Yu, J. Hu, J. Tan, Y. Gao, Y. Lu, F. Xuan, *Nanotechnology* **2018**, 29, 115502.
- [105] S. Luo, J. Yang, X. Song, X. Zhou, L. Yu, T. Sun, C. Yu, D. Huang, C. Du, D. Wei, *Solid-State Electron.* **2018**, 145, 29.
- [106] W. Cheng, J. Wang, Z. Ma, K. Yan, Y. Wang, H. Wang, S. Li, Y. Li, L. Pan, Y. Shi, *IEEE Electron Device Lett.* **2018**, 39, 288.
- [107] B. He, Z. Yan, Y. Zhou, J. Zhou, Q. Wang, Z. Wang, *J. Micromech. Microeng.* **2018**, 28, 105001.
- [108] Y. Joo, J. Byun, N. Seong, J. Ha, H. Kim, S. Kim, T. Kim, H. Im, D. Kim, Y. Hong, *Nanoscale* **2015**, 7, 6208.
- [109] C. M. Boutry, A. Nguyen, Q. O. Lawal, A. Chortos, S. Rondeau-Gagné, Z. Bao, *Adv. Mater.* **2015**, 27, 6954.
- [110] S. Y. Kim, S. Park, H. W. Park, D. H. Park, Y. Jeong, D. H. Kim, *Adv. Mater.* **2015**, 27, 4178.
- [111] D. H. Ho, Q. Sun, S. Y. Kim, J. T. Han, D. H. Kim, J. H. Cho, *Adv. Mater.* **2016**, 28, 2601.
- [112] Z. Zhu, R. Li, T. Pan, *Adv. Mater.* **2018**, 30, 1705122.
- [113] W. Asghar, F. Li, Y. Zhou, Y. Wu, Z. Yu, S. Li, D. Tang, X. Han, J. Shang, Y. Liu, R. W. Li, *Adv. Mater. Technol.* **2020**, 5, 1900934.
- [114] J. Yang, S. Luo, X. Zhou, J. Li, J. Fu, W. Yang, D. Wei, *ACS Appl. Mater. Interfaces* **2019**, 11, 14997.
- [115] H. Han, S. Baik, B. Xu, J. Seo, S. Lee, S. Shin, J. Lee, J. H. Koo, Y. Mei, C. Pang, T. Lee, *Adv. Funct. Mater.* **2017**, 27, 170618.
- [116] Q. Zhou, B. Ji, Y. Wei, B. Hu, Y. Gao, Q. Xu, J. Zhou, B. Zhou, *J. Mater. Chem. A* **2019**, 7, 27334.
- [117] S. Sterbing-D'Angelo, M. Chadha, C. Chiu, B. Falk, W. Xian, J. Barcelo, J. M. Zook, C. F. Moss, *Proc. Natl. Acad. Sci. USA* **2011**, 108, 11291.
- [118] Y. M. Song, Y. Xie, V. Malyarchuk, J. Xiao, I. Jung, K. J. Choi, Z. Liu, H. Park, C. Lu, R. H. Kim, R. Li, K. B. Crozier, Y. Huang, J. A. Rogers, *Nature* **2013**, 497, 95.
- [119] J. Park, Y. Y. Lee, J. Hong, Y. Y. Lee, M. Ha, Y. Jung, H. Lim, S. Y. Kim, H. Ko, *ACS Nano* **2014**, 8, 12020.
- [120] A. A. Blandin, I. Bernardeschi, L. Beccai, *Biomimetics* **2018**, 3, 32.
- [121] T. Takahashi, M. Suzuki, S. Iwamoto, S. Aoyagi, *Micromachines* **2012**, 3, 270.
- [122] M. Y. Cheng, C. L. Lin, Y. T. Lai, Y. J. Yang, *Sensors* **2010**, 10, 10211.

- [123] A. A. Blandin, M. Totaro, I. Bernardeschi, in *Conference on Biomimetic and Biohybrid Systems, Living Machines 2017*, Vol. 10384 (Eds: M. Mangan, M. Cutkosky, A. Mura, P. F. M. J. Verschure, T. Prescott, N. Lepora), Springer, Cham, Switzerland **2017**, pp. 25–34.
- [124] S. Miller, Z. Bao, *J. Mater. Res.* **2015**, *30*, 3584.
- [125] S. Kang, J. Lee, S. Lee, S. G. Kim, J. K. Kim, H. Algadi, S. Al-Sayari, D. E. Kim, D. E. Kim, T. Lee, *Adv. Electron. Mater.* **2016**, *2*, 1600356.
- [126] J. O. Kim, S. Y. Kwon, Y. Kim, H. B. Choi, J. C. Yang, J. Oh, H. S. Lee, J. Y. Sim, S. Ryu, S. Park, *ACS Appl. Mater. Interfaces* **2019**, *11*, 1503.
- [127] F. Cote, R. Biagi, H. Bart-Smith, V. S. Deshpande, *Int. J. Solids Struct.* **2007**, *44*, 3533.
- [128] P. Wei, X. Guo, X. Qiu, D. Yu, *Nanotechnology* **2019**, *30*, 455501.
- [129] S. Wan, H. Bi, Y. Zhou, X. Xie, S. Su, K. Yin, L. Sun, *Carbon* **2017**, *114*, 209.
- [130] Y. N. Zheng, Z. Yu, G. Mao, Y. Li, D. Pravarthana, W. Asghar, Y. Liu, S. Qu, J. Shang, R. W. Li, *Global Challenges* **2020**, *4*, 1900079.
- [131] C. Metzger, E. Fleisch, J. Meyer, M. Dansachmüller, I. Graz, M. Kaltenbrunner, C. Keplinger, R. Schwödiauer, S. Bauer, *Appl. Phys. Lett.* **2008**, *92*, 2006.
- [132] S. Chen, B. Zhuo, X. Guo, *ACS Appl. Mater. Interfaces* **2016**, *8*, 20364.
- [133] J. Tao, M. Dong, L. Li, C. Wang, J. Li, Y. Liu, R. Bao, C. Pan, *Microsyst. Nanoeng.* **2020**, *6*, 62.
- [134] C. Pang, G. Y. Lee, T. Il Kim, S. M. Kim, H. N. Kim, S. H. Ahn, K. Y. Suh, *Nat. Mater.* **2012**, *11*, 795.
- [135] B. Zhu, Z. Niu, H. H. Wang, W. R. Leow, H. H. Wang, Y. Li, L. Zheng, J. Wei, F. Huo, X. Chen, *Small* **2014**, *10*, 3625.
- [136] G. Schwartz, B. C. K. Tee, J. Mei, A. L. Appleton, D. H. Kim, H. Wang, Z. Bao, *Nat. Commun.* **2013**, *4*, 6954.
- [137] S. Peng, S. Wu, Y. Yu, B. Xia, N. Lovell, C. H. Wang, *ACS Appl. Mater. Interfaces* **2020**, *12*, 22179.
- [138] S. P. Lacour, S. Benmerah, E. Tarte, J. Fitzgerald, J. Serra, S. McMahon, J. Fawcett, O. Graudejus, Z. Yu, B. Morrison, *Med. Biol. Eng. Comput.* **2010**, *48*, 945.
- [139] Y. Wan, Z. Qiu, J. Huang, J. Yang, Q. Wang, P. Lu, J. Yang, J. Zhang, S. Huang, Z. Wu, C. F. Guo, *Small* **2018**, *14*, 1801657.
- [140] L. Wang, K. Wang, Z. Lou, K. Jiang, G. Shen, *Adv. Funct. Mater.* **2018**, *28*, 1804501.
- [141] L. Feng, S. Li, Y. Li, H. Li, L. Zhang, J. Zhai, Y. Song, B. Liu, L. Jiang, D. Zhu, *Adv. Mater.* **2002**, *14*, 1857.
- [142] C. Mahata, H. Algadi, J. Lee, S. Kim, T. Lee, *Measurement* **2020**, *151*, 107095.
- [143] S. Rachel, A. Ruth, Z. Bao, *ACS Appl. Mater. Interfaces* **2020**, *12*, 58301.
- [144] J. C. Yang, J. O. Kim, J. Oh, S. Y. Kwon, J. Y. Sim, D. W. Kim, H. B. Choi, S. Park, *ACS Appl. Mater. Interfaces* **2019**, *11*, 19472.
- [145] Y. Shu, H. Tian, Y. Yang, C. Li, Y. Cui, W. Mi, Y. Li, Z. Wang, N. Deng, B. Peng, T. L. Ren, *Nanoscale* **2015**, *7*, 8636.
- [146] Y. Luo, J. Shao, S. Chen, X. Chen, H. Tian, X. Li, L. Wang, D. Wang, B. Lu, *ACS Appl. Mater. Interfaces* **2019**, *11*, 17796.
- [147] T. Sekitani, H. Nakajima, H. Maeda, T. Fukushima, T. Aida, K. Hata, T. Someya, *Nat. Mater.* **2009**, *8*, 494.
- [148] T. Fukushima, A. Kosaka, Y. Ishimura, T. Yamamoto, T. Takigawa, N. Ishii, T. Aida, *Science* **2003**, *300*, 2072.
- [149] W. Cheng, L. Yu, D. Kong, Z. Yu, H. Wang, Z. Ma, Y. Wang, J. Wang, L. Pan, Y. Shi, *IEEE Electron Device Lett.* **2018**, *39*, 1069.
- [150] M. Y. Cheng, X. H. Huang, C. W. Ma, Y. J. Yang, *J. Micromech. Microeng.* **2009**, *19*, 115001.
- [151] R. Li, Y. Si, Z. Zhu, Y. Guo, Y. Zhang, N. Pan, G. Sun, T. Pan, *Adv. Mater.* **2017**, *29*, 1700253.
- [152] J. Shi, S. Liu, L. Zhang, B. Yang, L. Shu, Y. Yang, M. Ren, Y. Wang, J. Chen, W. Chen, Y. Chai, X. Tao, *Adv. Mater.* **2020**, *32*, 1901958.
- [153] T. Yang, D. Xie, Z. Li, H. Zhu, *Mater. Sci. Eng., R* **2017**, *115*, 1.
- [154] T. Q. Trung, N. E. Lee, *Adv. Mater.* **2016**, *28*, 4338.
- [155] M. X. Wang, Y. M. Chen, Y. Gao, C. Hu, J. Hu, L. Tan, Z. Yang, *ACS Appl. Mater. Interfaces* **2018**, *10*, 26610.
- [156] S. Chung, J. Lee, H. Song, S. Kim, J. Jeong, Y. Hong, *Appl. Phys. Lett.* **2011**, *98*, 153110.
- [157] N. Gao, X. Zhang, S. Liao, H. Jia, Y. Wang, *ACS Macro Lett.* **2016**, *5*, 823.
- [158] S. Baek, H. Jang, S. Y. Kim, H. Jeong, S. Han, Y. Jang, D. H. Kim, H. S. Lee, *RSC Adv.* **2017**, *7*, 39420.
- [159] O. Atalay, A. Atalay, J. Gafford, H. Wang, R. Wood, C. Walsh, *Adv. Mater. Technol.* **2017**, *2*, 1700081.
- [160] T. Pickering, J. M. Hamm, A. F. Page, S. Wuestner, O. Hess, *Nat. Commun.* **2014**, *5*, 4972.
- [161] Y. Su, X. Ping, K. J. Yu, J. W. Lee, J. A. Fan, B. Wang, M. Li, R. Li, D. V. Harburg, Y. A. Huang, C. Yu, S. Mao, J. Shim, Q. Yang, P. Y. Lee, A. Armonas, K. J. Choi, Y. Yang, U. Paik, T. Chang, T. J. Dawidczyk, Y. A. Huang, S. Wang, J. A. Rogers, *Adv. Mater.* **2017**, *29*, 1604989.
- [162] F. Xu, W. Lu, Y. Zhu, *ACS Nano* **2011**, *5*, 672.
- [163] Y. Sun, V. Kumar, I. Adesida, J. A. Rogers, *Adv. Mater.* **2006**, *18*, 2857.
- [164] N. Bowden, S. Brittain, A. G. Evans, J. W. Hutchinson, G. M. Whitesides, *Nature* **1998**, *393*, 146.
- [165] D. S. Gray, J. Tien, C. S. Chen, *Adv. Mater.* **2004**, *16*, 393.
- [166] Y. Wang, Q. Liu, J. Zhang, T. Hong, W. Sun, L. Tang, E. Arnold, Z. Suo, W. Hong, Z. Ren, C. F. Guo, *Adv. Mater.* **2019**, *31*, 1902955.
- [167] S. Chen, K. Jiang, Z. Lou, D. Chen, G. Shen, *Adv. Mater. Technol.* **2018**, *3*, 1700248.
- [168] J. A. Rogers, R. Ghaffari, D. H. Kim, *Stretchable Bioelectronics for Medical Devices and Systems*, Springer, Cham **2016**.
- [169] S. Zhao, J. Li, D. Cao, G. Zhang, J. Li, K. Li, Y. Yang, W. Wang, Y. Jin, R. Sun, C. P. Wong, *ACS Appl. Mater. Interfaces* **2017**, *9*, 12147.
- [170] M. Watanabe, H. Shirai, T. Hirai, *J. Appl. Phys.* **2002**, *92*, 4631.
- [171] Z. Y. Huang, W. Hong, Z. Suo, *J. Mech. Phys. Solids* **2005**, *53*, 2101.
- [172] J. Song, H. Jiang, Z. J. Liu, D. Y. Khang, Y. Huang, J. A. Rogers, C. Lu, C. G. Koh, *Int. J. Solids Struct.* **2008**, *45*, 3107.
- [173] J. Jeong, S. Kim, J. Cho, Y. Hong, *IEEE Electron Device Lett.* **2009**, *30*, 1284.
- [174] M. Benslimane, P. Gravesen, P. Sommer-Larsen, *Proc. SPIE* **2002**, *4695*, 150.
- [175] M. Benslimane, H.-E. Kiil, M. J. Tryson, *Proc. SPIE* **2010**, *7642*, 764231.
- [176] D. C. Duffy, J. C. McDonald, O. J. A. Schueller, G. M. Whitesides, *Anal. Chem.* **1998**, *70*, 4974.
- [177] Y. Sun, J. A. Rogers, *Nano Lett.* **2004**, *4*, 1953.
- [178] Y. Y. Huang, W. Zhou, K. J. Hsia, E. Menard, J. U. Park, J. A. Rogers, A. G. Alleyne, *Langmuir* **2005**, *21*, 8058.
- [179] Y. Sun, W. M. Choi, H. Jiang, Y. Y. Huang, J. A. Rogers, *Nat. Nanotechnol.* **2006**, *1*, 201.
- [180] D. Y. Y. Khang, H. Jiang, Y. Huang, J. A. Rogers, *Science* **2006**, *311*, 208.
- [181] H. Jiang, D. Y. Khang, J. Song, Y. Sun, Y. Huang, J. A. Rogers, *Proc. Natl. Acad. Sci. USA* **2007**, *104*, 15607.
- [182] J. Kim, E. F. Chou, J. Le, S. Wong, M. Chu, M. Khine, *Adv. Healthcare Mater.* **2019**, *8*, 1900109.
- [183] L. Ma, X. Shuai, Y. Hu, X. Liang, P. Zhu, R. Sun, C. P. Wong, *J. Mater. Chem. C* **2018**, *6*, 13232.
- [184] S. Chen, S. Peng, W. Sun, G. Gu, Q. Zhang, X. Guo, *Adv. Mater. Technol.* **2019**, *4*, 1800681.
- [185] W. M. Choi, J. Song, D. Y. Khang, H. Jiang, Y. Y. Huang, J. A. Rogers, *Nano Lett.* **2007**, *7*, 1655.
- [186] Z. F. Liu, S. Fang, F. A. Moura, J. N. Ding, N. Jiang, J. Di, M. Zhang, X. Lepró, D. S. Galvão, C. S. Haines, N. Y. Yuan, S. G. Yin, D. W. Lee, R. Wang, H. Y. Wang, W. Lv, C. Dong, R. C. Zhang,

- M. J. Chen, Q. Yin, Y. T. Chong, R. Zhang, X. Wang, M. D. Lima, R. Ovalle-Robles, D. Qian, H. Lu, R. H. Baughman, *Science* **2015**, 349, 400.
- [187] Y. Wei, S. Chen, X. Yuan, P. Wang, L. Liu, *Adv. Funct. Mater.* **2016**, 26, 5078.
- [188] F. Arab Hassani, H. Jin, T. Yokota, T. Someya, N. V. Thakor, *Sci. Adv.* **2020**, 6, eaba0412.
- [189] D. H. Kim, J. A. Rogers, *Adv. Mater.* **2008**, 20, 4887.
- [190] S. Kim, S. Choi, E. Oh, J. Byun, H. Kim, B. Lee, S. Lee, Y. Hong, *Sci. Rep.* **2016**, 6, 34632.
- [191] D. H. Kim, J. Song, M. C. Won, H. S. Kim, R. H. Kim, Z. Liu, Y. Y. Huang, K. C. Hwang, Y. W. Zhang, J. A. Rogers, *Proc. Natl. Acad. Sci. USA* **2008**, 105, 18675.
- [192] D. J. Lipomi, B. C. K. Tee, M. Vosgueritchian, Z. Bao, *Adv. Mater.* **2011**, 23, 1771.
- [193] Y. Kim, A. Chortos, W. Xu, Y. Liu, J. Y. Oh, D. Son, J. Kang, A. M. Foudeh, C. Zhu, Y. Lee, S. Niu, J. Liu, R. Pfattner, Z. Bao, T. W. Lee, *Science* **2018**, 360, 998.
- [194] Y. Cho, J. H. Shin, A. Costa, T. A. Kim, V. Kunin, J. Li, S. Y. Lee, S. Yang, H. N. Han, I. S. Choi, D. J. Srolovitz, *Proc. Natl. Acad. Sci. USA* **2014**, 111, 17390.
- [195] Y. Su, J. Wu, Z. Fan, K. C. Hwang, J. Song, Y. Huang, J. A. Rogers, *J. Mech. Phys. Solids* **2012**, 60, 487.
- [196] J. A. Fan, W. H. Yeo, Y. Su, Y. Hattori, W. Lee, S. Y. Jung, Y. Zhang, Z. Liu, H. Cheng, L. Falgout, M. Bajema, T. Coleman, D. Gregoire, R. J. Larsen, Y. Huang, J. A. Rogers, *Nat. Commun.* **2014**, 5, 3266.
- [197] S. Huang, Y. Liu, Y. Zhao, Z. Ren, C. F. Guo, *Adv. Funct. Mater.* **2019**, 29, 1805924.
- [198] S. Gong, W. Cheng, *Adv. Electron. Mater.* **2017**, 3, 1600314.
- [199] J. A. Rogers, T. Someya, Y. Huang, J. A. Rogers, T. Someya, Y. Huang, *Science* **2010**, 327, 1603.
- [200] T. Pan, M. Pharr, Y. Ma, R. Ning, Z. Yan, R. Xu, X. Feng, Y. Huang, J. A. Rogers, *Adv. Funct. Mater.* **2017**, 27, 1702589.
- [201] Y. Zhang, S. Xu, H. Fu, J. Lee, J. Su, K. C. Hwang, J. A. Rogers, Y. Huang, *Soft Matter* **2013**, 9, 8062.
- [202] H. Wei, K. Li, W. G. Liu, H. Meng, P. X. Zhang, C. Y. Yan, *Adv. Eng. Mater.* **2017**, 19, 1700341.
- [203] J. Kim, M. Lee, H. J. Shim, R. Ghaffari, H. R. Cho, D. Son, Y. H. Jung, M. Soh, C. Choi, S. Jung, K. Chu, D. Jeon, S. T. Lee, J. H. Kim, S. H. Choi, T. Hyeon, D. H. Kim, *Nat. Commun.* **2014**, 5, 5747.
- [204] X. Zhao, Q. Hua, R. Yu, Y. Zhang, C. Pan, *Adv. Electron. Mater.* **2015**, 1, 1500142.
- [205] F. Xu, Y. Zhu, *Adv. Mater.* **2012**, 24, 5117.
- [206] J. W. Jeong, W. H. Yeo, A. Akhtar, J. J. S. Norton, Y. J. Kwack, S. Li, S. Y. Jung, Y. Su, W. Lee, J. Xia, H. Cheng, Y. Huang, W. S. Choi, T. Bretl, J. A. Rogers, *Adv. Mater.* **2013**, 25, 6839.
- [207] W. H. Yeo, Y. S. Kim, J. Lee, A. Ameen, L. Shi, M. Li, S. Wang, R. Ma, S. H. Jin, Z. Kang, Y. Huang, J. A. Rogers, *Adv. Mater.* **2013**, 25, 2773.
- [208] D. Son, J. Lee, S. Qiao, R. Ghaffari, J. Kim, J. E. Lee, C. Song, S. J. Kim, D. J. Lee, S. W. Jun, S. Yang, M. Park, J. Shin, K. Do, M. Lee, K. Kang, C. S. Hwang, N. Lu, T. Hyeon, D. H. Kim, *Nat. Nanotechnol.* **2014**, 9, 397.
- [209] Q. Hua, J. Sun, H. Liu, R. Bao, R. Yu, J. Zhai, C. Pan, Z. L. Wang, *Nat. Commun.* **2018**, 9, 244.
- [210] D. H. Kim, J. H. Ahn, M. W. Choi, H. S. Kim, T. H. Kim, J. Z. Song, Y. Huang, Z. J. Liu, C. Lu, J. A. Rogers, *Science* **2008**, 320, 507.
- [211] C. F. Guo, T. Sun, Q. Liu, Z. Suo, Z. Ren, *Nat. Commun.* **2014**, 5, 3121.
- [212] A. P. Gerratt, H. O. Michaud, S. P. Lacour, *Adv. Funct. Mater.* **2015**, 25, 2287.
- [213] C. B. Cooper, K. Arutselvan, Y. Liu, D. Armstrong, Y. Lin, M. R. Khan, J. Genzer, M. D. Dickey, *Adv. Funct. Mater.* **2017**, 27, 1605630.
- [214] Y. Cheng, R. Wang, H. Zhai, J. Sun, *Nanoscale* **2017**, 9, 3834.
- [215] L. Wang, J. A. Jackman, E. L. Tan, J. H. Park, M. G. Potroz, E. T. Hwang, N. J. Cho, *Nano Energy* **2017**, 36, 38.
- [216] Z. Yang, Y. Pang, X. L. Han, Y. Yang, Y. Yang, J. Ling, M. Jian, Y. Zhang, T. L. Ren, *ACS Nano* **2018**, 12, 9134.
- [217] S. Lee, A. Reuveny, J. Reeder, S. Lee, H. Jin, Q. Liu, T. Yokota, T. Sekitani, T. Isoyama, Y. Abe, Z. Suo, T. Someya, *Nat. Nanotechnol.* **2016**, 11, 472.
- [218] Y. Li, Y. A. Samad, T. Taha, G. Cai, S. Y. Fu, K. Liao, *ACS Sustainable Chem. Eng.* **2016**, 4, 4288.
- [219] S. Gong, W. Schwalb, Y. Wang, Y. Chen, Y. Tang, J. Si, B. Shirinzadeh, W. Cheng, *Nat. Commun.* **2014**, 5, 3132.
- [220] F. Wang, S. Liu, L. Shu, X. M. Tao, *Carbon* **2017**, 121, 353.
- [221] H. Jin, M. O. G. Nayeem, S. Lee, N. Matsuhisa, D. Inoue, T. Yokota, D. Hashizume, T. Someya, *ACS Nano* **2019**, 13, 7905.
- [222] H. Zhao, L. Hou, J. X. Wu, Y. X. Lu, *J. Mater. Chem. C* **2016**, 4, 7156.
- [223] Y. Liu, S. Gorgutsa, C. Santato, M. Skorobogatiy, *J. Electrochem. Soc.* **2012**, 159, A349.
- [224] B. He, Y. Zhou, Z. Wang, Q. Wang, R. Shen, S. Wu, *Sens. Actuators, A* **2018**, 272, 341.
- [225] A. Schmitz, P. Maiolino, M. Maggiali, L. Natale, G. Cannata, G. Metta, *IEEE Trans. Rob.* **2011**, 27, 389.
- [226] T. Q. Trung, N. E. Lee, *Adv. Mater.* **2017**, 29, 1603167.
- [227] H. B. Lee, C. W. Bae, L. T. Duy, I. Y. Sohn, D. Il Kim, Y. J. Song, Y. J. Kim, N. E. Lee, *Adv. Mater.* **2016**, 28, 3069.
- [228] Y. Cheng, R. Wang, J. Sun, L. Gao, *Adv. Mater.* **2015**, 27, 7365.
- [229] S. H. Cho, S. W. Lee, S. Yu, H. Kim, S. Chang, D. Kang, I. Hwang, H. S. Kang, B. Jeong, E. H. Kim, S. M. Cho, K. L. Kim, H. Lee, W. Shim, C. Park, *ACS Appl. Mater. Interfaces* **2017**, 9, 10128.
- [230] J. Kim, T. N. Ng, W. S. Kim, *Appl. Phys. Lett.* **2012**, 101, 103308.
- [231] K. F. Lei, K. F. Lee, M. Y. Lee, *Microsyst. Technol.* **2014**, 20, 1351.
- [232] P. Maiolino, F. Galantini, F. Mastrogiiovanni, G. Gallone, G. Cannata, F. Carpi, *Sens. Actuators, A* **2015**, 226, 37.
- [233] O. Atalay, A. Atalay, J. Gafford, C. Walsh, *Adv. Mater. Technol.* **2018**, 3, 1700237.
- [234] Z. Qiu, Y. Wan, W. Zhou, J. Yang, J. Yang, J. Huang, J. Zhang, Q. Liu, S. Huang, N. Bai, Z. Wu, W. Hong, H. Wang, C. F. Guo, *Adv. Funct. Mater.* **2018**, 28, 1802343.
- [235] L. Ma, X. Yu, Y. Yang, Y. Hu, X. Zhang, H. Li, X. Ouyang, P. Zhu, R. Sun, C. P. Wong, *J. Mater.* **2020**, 6, 321.
- [236] T. H. Park, S. Yu, S. H. Cho, H. S. Kang, Y. Kim, M. J. Kim, H. Eoh, C. Park, B. Jeong, S. W. Lee, D. Y. Ryu, J. Huh, C. Park, *NPG Asia Mater.* **2018**, 10, 328.



Jing Qin is a postgraduate student in the School of Science, Beijing University of Posts and Telecommunications, China. Her research interest is nanocomposite dielectrics for flexible and stretchable capacitive sensors.



Ya-Nan Hao received her Ph.D. degree from Tsinghua University in 2016. She is now an associate professor in Beijing University of Posts and Telecommunications. Her research interests are focused on nanoscaled perovskite materials and their application in microelectronics and energy storage, information functional materials, and devices.



Zhi-Min Dang received his Ph.D. degree in electrical engineering from Xi'an Jiaotong University in 2001. He is currently a professor in the Department of Electrical Engineering, Tsinghua University. His research interests are advanced energy/electrical materials and devices. He has published more than 270 journal papers with a current citation record of over 13 000 times and an H-index of 59.